



# Abnormal Evolution of Pitting Behavior of Warmly Pre-Strained Austenitic Stainless Steels

Huimin Tao, Chengshuang Zhou, Yuanjian Hong, Kaiyu Zhang, Lin Zhang, and Jinyang Zheng

Submitted: 20 July 2020 / Revised: 9 October 2020 / Accepted: 26 October 2020 / Published online: 9 November 2020

The effect of warm pre-strain on the corrosion behavior of 304 and 316 steels in 3.5% NaCl solution was first explored by electrochemical tests, passive film characterization, and structural analysis. The pitting corrosion resistance of 304 steel decreases with the increase of strain level below 20% and increases with the strain at a higher strain level, while the pitting corrosion resistance of 316 steel increases slightly with the increase of strain level below 20% and decreases with the strain at a higher strain level. The random grain boundaries in 304 steel are interrupted with the increase of strain level higher than 20%; this does not occur in 316 steel, which exhibits more dislocations. The coupling effect of microstructure changes induced by warm pre-strain affects the oxide content of the passive film, especially for the chromium oxide, which results in abnormal corrosion behavior. Knowing the corrosion mechanism is of value for academic research and enables the design of advanced stainless steel with high strength and corrosion resistance.

**Keywords** corrosion behavior, passive film, polarization, stainless steel, structures, XPS

## 1. Introduction

Austenitic stainless steels (including types 304, 316, and 310S) are widely used in the industrial field because they are rich in varieties, reasonably priced, technically efficient, and environmentally friendly (Ref 1-3). Nevertheless, austenitic stainless steels are extremely sensitive to local corrosion, which will lead to failure of industrial components (Ref 4-6). Thus, the corrosion problem of austenitic stainless steel in industrial application should not be ignored. In general, the properties of austenitic stainless steel depend mostly on its composition and structure. In (Ref 7), it was reported that the addition of Mo can improve the quality of oxide film on the surface of stainless steel, because the formation of Mo-insoluble compounds promotes the repassivation of pit and prevents from corrosion. However, the addition of the Mn will increase the MnS content in stainless steel, which easily causes local corrosion. Some researchers have focused on the influence of structure on the properties of stainless steel. Structural changes comprise the development of, for example, subgrains, grain boundaries, and dislocations, which are typical for stainless steel. In addition, the martensite phase, twins, and dislocation induced by strain can distinctly improve the yield strength of austenitic stainless steels (Ref 8). The strengthening contributions of martensite and austenite phases may be similar, and the dislocation is much higher than that of the grain boundary. Based on the

existing research reports, much effort has been devoted to improving the properties of stainless steel by controlling their compositions or structures. Some researchers have improved the localized corrosion resistance of stainless steel in aggressive environments by adding the alloying elements Mo, Cr, and N (Ref 9-11). Other researchers have adjusted the structure of stainless steel during manufacturing to change the properties, which is also called ‘materials plainification’ (Ref 12). Compared with changing the composition of stainless steel, manufacturing can reduce resource consumption and production costs; also, the process is highly controllable, and the materials are recyclable. Hence, manufacturing presents superior prospects for optimizing the properties of stainless steel.

Among numerous manufacturing technologies, rolling is practical and effective for adjusting the properties of metals, and some progress has been made in the research field of rolled stainless steel (Ref 13-16). Generally, the strain of stainless steel can be classified into cold, warm, and hot strain levels according to the different strain temperatures. The strain in stainless steel occurring below the recovery temperature is classified as cold strain, the strain occurring over the recovery temperature but below the recrystallization temperature is classified as warm strain, and the strain occurring over the recrystallization temperature is classified as hot strain. According to (Ref 14), both the martensite phase and refined grains produced by cold-rolling can strengthen 304 stainless steel, while only refined grains have this effect on 316 stainless steel. In 316 stainless steel treated with 900 °C hot-rolling, strain substructures barely develop at a low strain level, while they develop well in most grains at a high strain level. Also, the grain size becomes finer, and the misorientation angle increases with the strain level (Ref 15). Unfortunately, most researchers from the previously mentioned studies have focused on the cold or hot strain in stainless steel, while the warm strain has been rarely investigated. Because the material properties strongly depend on the strain temperature, investigating the warm strain may provide a new path for improving the material properties. According to (Ref 17, 18), the warm strain state can be used to overcome some deficiencies of the cold strain state; thus, it has a wide application prospect for stainless steel. However, warm-

Huimin Tao, Chengshuang Zhou, Yuanjian Hong, Kaiyu Zhang, and Lin Zhang, Institute of Material Forming and Control Engineering, Zhejiang University of Technology, Hangzhou 310014, China; and Jinyang Zheng, Institute of Chemical Machinery Engineering, Zhejiang University, Hangzhou 310027, China. Contact e-mails: zhlin@zjut.edu.cn and jyzh@zju.edu.cn.

strained stainless steels have not been thoroughly studied owing to their complexity. Besides, the corrosion mechanism of stainless steel needs to be clarified for future industrial applications.

In this study, the effects of warm-rolling (temperature: 200 °C, strain level: 0 to 50%) on the corrosion properties of 304 and 316 steels in 3.5% NaCl solution were studied. The corrosion behavior of warm pre-strained 304 and 316 steels was studied first, and the corrosion mechanism was discussed based on the strain-induced structures and characteristics of the passive film.

## 2. Experimental

The chemical composition of the 304 and 316 steels used in this work are listed in Table 1. The pitting resistance equivalent (PRE) index of stainless steels can be empirically evaluated with the equation:  $PRE\ index = 16\%N + 3.3\%Mo + 1.0\%Cr$  (Ref 19). Through calculation, the PRE index of 304 steel (approximately 18.44) is smaller than that of 316 steel (approximately 24.43). The prepared materials were annealed at 1050 °C for 1 h in the vacuum furnace and then quenched rapidly in the water to avoid sensitization. The sensitization of stainless steel generally occurs in the long-term heating process of 450-850 °C, which will affect its properties (Ref 20, 21). The annealed steel plates were repeatedly unidirectionally rolled to reduce their thickness from 10 to 50%. Moreover, all rollers and steel plates were reheated to 200 °C after each warm-rolling progress. The details of the rolling strain process are presented in Fig. 1. The samples were extracted from the annealed and corresponding pre-strained plates. For example, the 304-10% sample was obtained from the 304 steel plate, which was rolled until a thickness reduction of 10% was reached at 200 °C. The samples were marked with the rolling direction (RD) and transverse direction (TD).

The electrochemical tests were performed with an IviumStat electrochemical workstation; the counter electrode consisted of platinum foil, the reference electrode was a saturated calomel electrode (SCE) (the potentials mentioned below were converted to the reference electrode potential), and the working electrode consisted of the prepared samples. For the corrosion tests, the samples were embedded in plastic tubing with araldite adhesive after they were soldered with insulated copper wire on their backs. The working area of the samples exposed to the medium was approximately 1 cm<sup>2</sup>. Each sample was sequentially ground with SiC sandpapers (up to 2000 grit) and then polished with 0.1 μm diamond paste. Before the tests, the samples were ultrasonically rinsed with alcohol and dried with dry air. In the potentiodynamic polarization tests, the samples that were previously immersed in the medium for 3600 s, experienced a potential sweep from (−600) mV to (+1000) mV

**Table 1 Chemical compositions of 304 and 316 steels used in this work (mass fraction/wt.%)**

Materials	Cr	Ni	Mo	Mn	Si	N	C	Fe
304	18.09	8.06	0.01	1.13	0.33	0.02	0.07	Bal.
316	16.6	10.2	2.13	1.17	0.56	0.05	0.02	Bal.

at a rate of (+0.2) mV/s. The related parameters of the potentiodynamic polarization plots, including the pitting potential ( $E_p$ ), passive current density ( $i_p$ ), corrosion potential ( $E_c$ ), and the range of the passive potential ( $\Delta E$ ,  $\Delta E = E_p - E_c$ ), were determined to analyze the evolution of corrosion properties of 304 and 316 samples. The  $E_p$  value was determined based on the point at which the current density sharply increased, and  $i_p$  was determined based on the center of the passive zone of the polarization plot. To study the metastable pitting corrosion behavior of the 304 and 316 samples, potentiostatic polarization tests were performed for 6000 s at a constant potential of +100 mV in the medium. All the electrochemical tests were conducted in a 3.5% NaCl solution. Electrochemical impedance spectroscopy (EIS) experiments were conducted in the frequency range of 100 kHz-10 mHz at the open circuit potential, and the amplitude was  $\pm 10$  mV. The test temperature was maintained at  $25 \pm 1$  °C by a thermostatic water bath to avoid the influence of temperature. The tests were repeated at least five times under each condition to guarantee the reliability, and the obtained result closest to the average value was taken as the final result of the analysis. The electrochemical studies of the intergranular corrosion were performed in a 10% oxalic acid reagent with an electricity density of 1 A/cm<sup>2</sup> for 90 s.

Furthermore, x-ray diffraction (XRD), electron backscatter diffraction (EBSD), and a nano-indenter were used to analyze the sample structures, and scanning electron microscopy (SEM), confocal laser scanning microscope, and optical microscopy were applied to analyze the surface topographies. Moreover, the characteristics of the passive films on the sample surfaces were explored by x-ray photoelectron spectroscopy (XPS).

## 3. Results

### 3.1 Electrochemical Corrosion Behavior

**3.1.1 Potentiodynamic Polarization Tests.** The results of the potentiodynamic polarization tests of the 304 and 316 steels with and without warm pre-strain are presented in Fig. 2, and the relevant information is presented in Tables 2 and 3. Regarding the 304 steel samples (Fig. 2a), the  $E_p$  decreased from 404.6 mV (304-0%) to 131.1 mV (304-20%) and then increased to 332.4 mV (304-50%) with increasing strain;  $i_p$  increased from 0.37 μA cm<sup>−2</sup> (304-0%) to 7.66 μA cm<sup>−2</sup> (304-20%) and then decreased to 1.50 μA cm<sup>−2</sup> (304-50%) with increasing strain. In addition,  $\Delta E$  decreased from 536.0 mV (304-0%) to the minimal value of 350.4 mV (304-20%) and then increased to 591.8 mV (304-50%) with increasing strain. Theoretically, the higher  $E_p$ ,  $\Delta E$ , and lower  $i_p$  of stainless steel indicate a better corrosion resistance and passivation ability (Ref 22-24). The results suggest that the pitting corrosion resistance of 304 steel first decreased with the increase of strain level below 20%, and then increased with the strain at a higher strain level. For the 316 samples (Fig. 2b), the  $E_p$  increased from 415.8 mV (316-0%) to 484.4 mV (316-20%) and then decreased to 229.9 mV (316-50%) with increasing strain;  $i_p$  decreased from 0.49 μA cm<sup>−2</sup> (316-0%) to 0.25 μA cm<sup>−2</sup> (316-20%) and then increased to 0.91 μA cm<sup>−2</sup> (316-50%). Besides,  $\Delta E$  increased from 541.8 mV (316-0%) to 592.5 mV (316-20%) and then decreased to 450.1 mV (316-50%) with

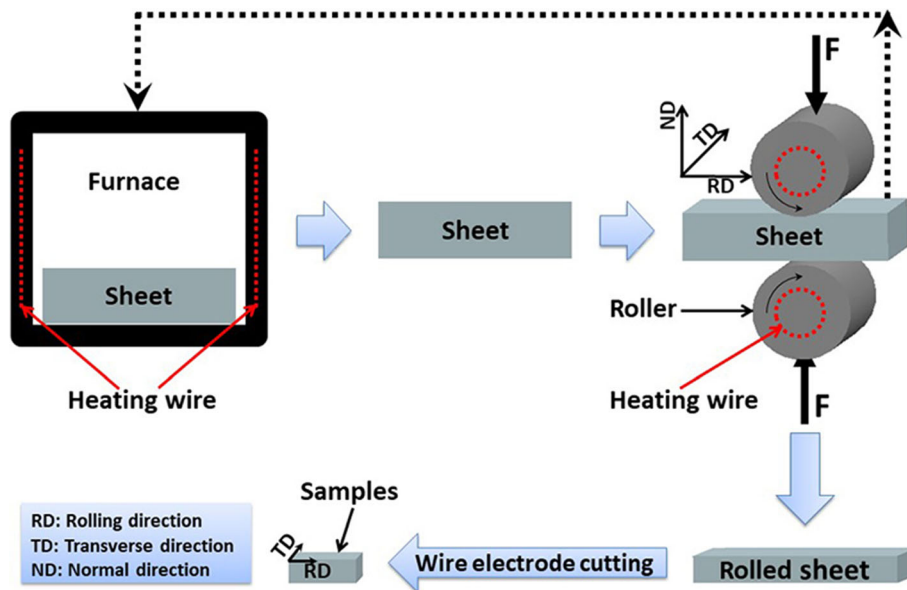


**Fig. 1** Diagram of warm-rolling strain process for 304 and 316 steels

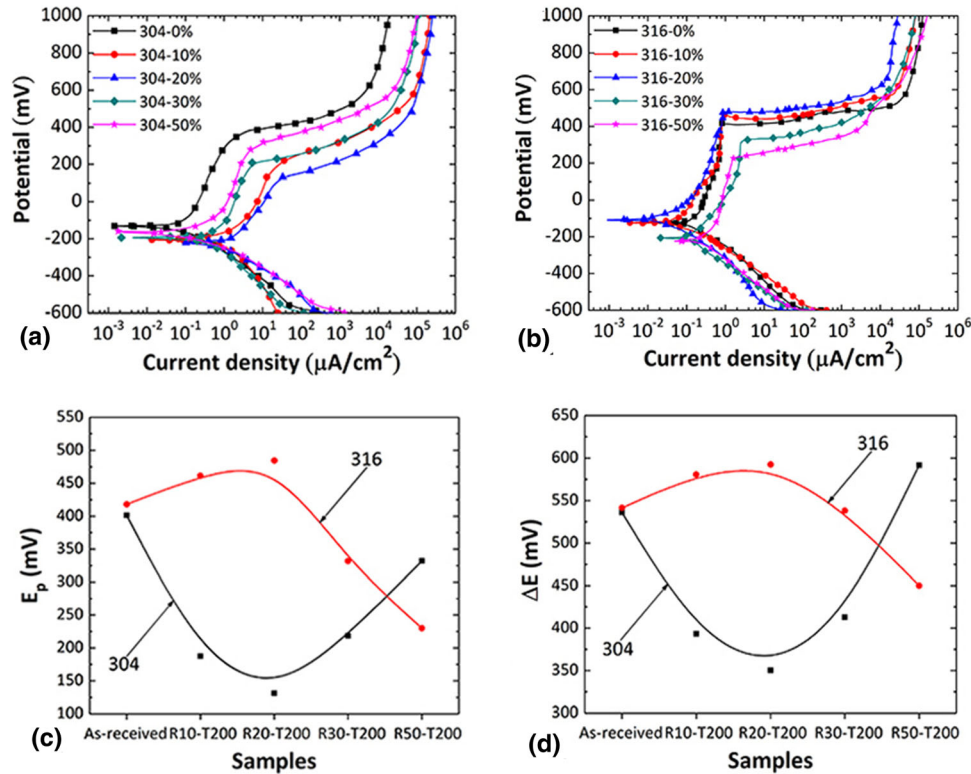


**Fig. 2** Potentiodynamic polarization plots of 304 and 316 samples in 3.5% NaCl solution at  $25 \pm 1$  °C.  $E_p$ : pitting potential,  $\Delta E$ : the range of the passive film stability potential

increasing strain. Hence, the pitting corrosion resistance of 316 steel first increased with the increase of strain level below 20% and decreased with the strain at a higher strain level. The detailed information of  $E_p$  and  $\Delta E$  of the samples is presented in Fig. 2(c) and (d). In summary, the pitting corrosion resistance of 304 steel decreased with the increase of strain level below 20% and increased with the strain at a higher strain

level, while the pitting corrosion resistance of 316 steel increased slightly with the increase of strain level below 20% and decreased with the strain at a higher strain level.

Surface micrographs and depth of corrosion pits of 304 and 316 samples after potentiodynamic polarization tests and the statistics of the initiated corrosion pits during potentiodynamic polarization tests are displayed in Fig. 3. As can be seen, the corrosive pits were elongated along the rolling direction with

**Table 2 Electrochemical test results of 304 samples in 3.5% NaCl solution at  $25 \pm 1$  °C**

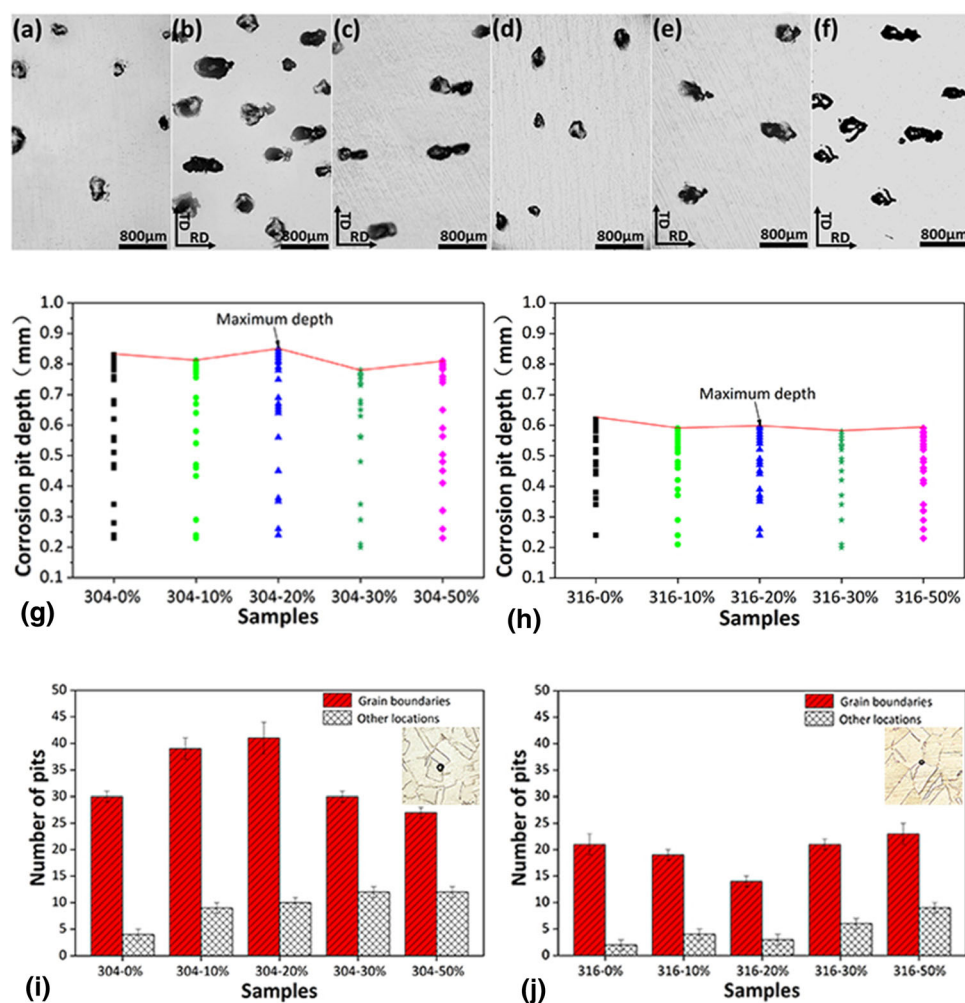
Samples	$E_p$ , mV	$i_p$ , $\mu\text{Acm}^{-2}$	$E_c$ , mV	$\Delta E$ , mV
304-0%	$404.6 \pm 5.2$	$0.37 \pm 0.02$	$-131.4 \pm 3.5$	$536.0 \pm 8.7$
304-10%	$187.5 \pm 5.9$	$7.36 \pm 0.04$	$-206.8 \pm 4.1$	$393.3 \pm 10.0$
304-20%	$131.1 \pm 1.7$	$7.66 \pm 0.03$	$-219.3 \pm 3.3$	$350.4 \pm 5.0$
304-30%	$218.3 \pm 5.2$	$1.55 \pm 0.03$	$-194.5 \pm 3.7$	$412.8 \pm 8.9$
304-50%	$332.4 \pm 6.3$	$1.50 \pm 0.04$	$-159.4 \pm 4.5$	$591.8 \pm 10.8$

$E_p$ : pitting potential,  $i_p$ : passive current density,  $E_c$ : corrosion potential,  $\Delta E$ : the range of the passive potential

**Table 3 Electrochemical test results of 316 samples in 3.5% NaCl solution at  $25 \pm 1$  °C**

Samples	$E_p$ , mV	$i_p$ , $\mu\text{Acm}^{-2}$	$E_c$ , mV	$\Delta E$ , mV
316-0%	$415.8 \pm 4.9$	$0.49 \pm 0.02$	$-125.6 \pm 2.4$	$541.4 \pm 7.3$
316-10%	$461.3 \pm 5.1$	$0.38 \pm 0.02$	$-119.3 \pm 2.5$	$580.6 \pm 7.6$
316-20%	$484.4 \pm 3.8$	$0.25 \pm 0.01$	$-108.1 \pm 2.5$	$592.5 \pm 6.3$
316-30%	$331.8 \pm 4.5$	$0.86 \pm 0.04$	$-206.3 \pm 3.7$	$538.1 \pm 8.2$
316-50%	$229.9 \pm 4.2$	$0.91 \pm 0.03$	$-220.2 \pm 4.1$	$450.1 \pm 8.3$

$E_p$ : pitting potential,  $i_p$ : passive current density,  $E_c$ : corrosion potential,  $\Delta E$ : the range of the passive potential

**Fig. 3** Surface micrographs of 304 and 316 samples after potentiodynamic polarization tests (a-f), statistics of corrosion pit depth of 304 and 316 samples after potentiodynamic polarization tests (g, h), and statistics of initiated corrosion pits during potentiodynamic polarization tests (i, j). (a), (b), and (c): 304-0%, 304-20%, and 304-50%; (d), (e), and (f): 316-0%, 316-20%, and 316-50%

increasing strain levels for both 304 and 316 samples (Fig. 3a and f). For 304 samples, the number of corrosion pits on the surface of 304 steel increased first with the increase of strain level below 20% and decreased with the strain at a higher strain level; clearly, the sample 304-20% had more corrosion pits than other samples. However, the number of corrosion pits on the surface of 316 steel slightly decreased first with the increase of strain level below 20% and increased with the strain at a higher strain level. The results of pits morphology observation also indicated that the pitting corrosion resistance of 304 steel increased first with the increase of strain level below 20% and decreased with the strain at a higher strain level, while the pitting corrosion resistance of 316 steel increased slightly with the increase of strain level below 20% and decreased with the strain at a higher strain level. Moreover, the depths of corrosion pits on the sample surfaces observed by the confocal laser scanning microscope are presented in Fig. 3(g) and (h). Clearly, the corrosion pit depths of 304 and 316 steel samples were approximately 0.25-0.85 mm and 0.20-0.60 mm, respectively. The maximum corrosion pit depth of 304 steel sample was greater than that of 316 steel sample at the same strain level, as the broken line in the figures. The maximum corrosion pit depth of 304 samples changed with the increase of strain level, and the sample 304-20% had the maximum corrosion pit depth compared with others, while strain slightly affected the maximum corrosion pit depth of 316 samples.

Moreover, the potentiodynamic polarization tests were stopped when the potential just passed through the  $E_p$  to investigate the preferential initiation locations of the corrosion pits. Each sample was tested for the same number of times. According to the statistical results of the initiated corrosion pits in Fig. 3(i) and (j), most corrosion pits occurred at the grain boundaries. Grain boundaries are defects in stainless steel, which can easily induce corrosion. Hence, the grain boundary of stainless steel may play a vital role in the corrosion behavior. Besides, the number of the initiated corrosion pits increased first and then decreased with the increase of strain level for 304 steel, while it decreased slightly first and then increased with the increase of strain level for 316 steel. The results are consistent with the above results of corrosion pit observation after potentiodynamic polarization tests.

**3.1.2 Potentiostatic Polarization Tests.** The potentiostatic polarization plots of the 304 and 316 steels with and without warm pre-strain are shown in Fig. 4. The transient

current densities of all samples first fluctuated and then gradually stabilized with time. In addition, some intermittent and vertical current fluctuation spikes occurred in the base plots, which were attributed to the thin or porous passive film formed on the sample surfaces and promoted the metastable pitting corrosion. Evidently, the trends of the relatively stable current values and current fluctuation spikes of the pre-strained 304 and 316 steels differ distinctly. For the 304 steel, the relatively stable current values increased first but then decreased with increasing strain, as shown in the illustration of Fig. 4a. Moreover, the relatively stable current value of sample 304-20% was higher than those of the others, and the densities and heights of the current fluctuation spikes of samples 304-10% and 304-20% were much greater than those of other samples. However, the relatively stable current values of samples 316-10% and 316-20% were as low as that of the 316-0% sample and increased with the strain (Fig. 4b). Furthermore, some current spikes appeared for the 316 samples at a higher strain level (30%-50%), whereas they did not appear for the other samples. In theory, the transient current density and fluctuant peaks reflect the metastable pitting corrosion behavior of samples. The samples with the lower transient current density and fewer fluctuant peaks revealed a slower electrochemical reaction activity of the metastable corrosion pits and a superior repassivation ability of the passive films on their surfaces (Ref 25-27). Thicker and denser passive films on sample surfaces hinder the diffusion of deleterious ions, which retards the metastable pitting reaction (Ref 28). Therefore, the metastable pitting resistance of the 304 steel decreased with the strain level below 20% and increased with the strain at a higher strain level that of 316 steel increased slightly with the increase of strain level below 20% and decreased significantly with the strain at a higher strain level.

**3.1.3 Electrochemical Impedance Spectroscopy.** Figure 5 shows the results of EIS tests of the 304 and 316 samples with and without warm pre-strain. The Nyquist plots of 304 and 316 samples are presented in Fig. 5(a) and (c), respectively. A similar semicircle shape over the whole frequency range in the Nyquist plots was observed. The semicircle diameters of the 304 samples decreased first with the increase of strain level below 20% and increased with the strain at a higher strain level (Fig. 5a). The semicircle diameters of the 316 samples increased first with the increase of strain level below 20% and decreased with the strain at a higher strain level

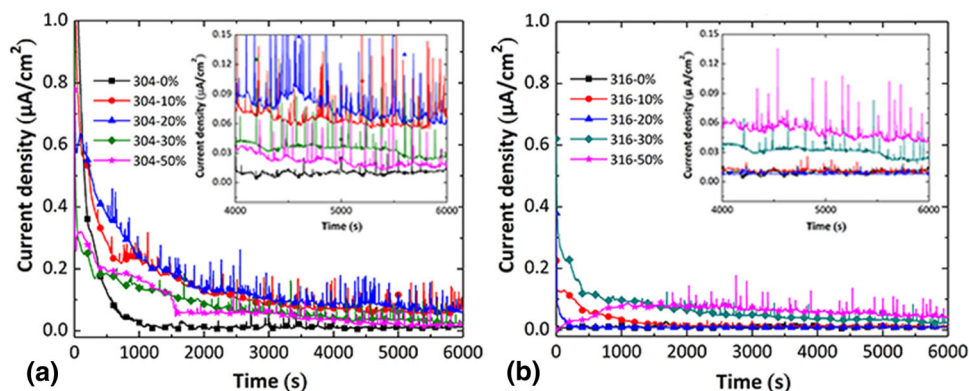


**Fig. 4** Potentiostatic polarization plots of 304 and 316 samples in 3.5% NaCl solution at  $25 \pm 1$  °C with the potential of 100 mV. The illustrations are partially enlarged views of the plots

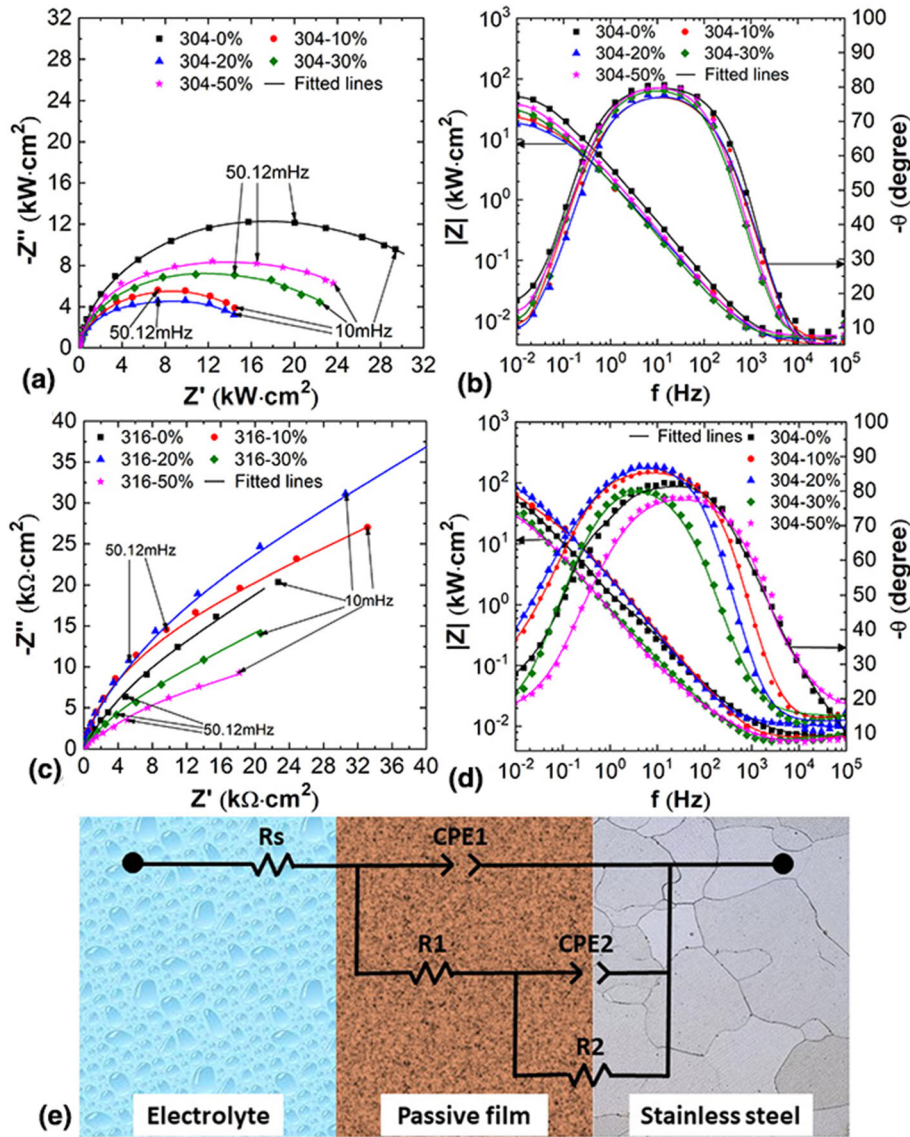


**Fig. 5** (a-d): Nyquist and Bode plots of the 304 and 316 samples with and without warm pre-strain. (e) Equivalent circuit model used to fit the impedance spectroscopy of the samples in 3.5 wt% NaCl solution

(Fig. 5b). Generally, the larger diameter of the semicircle indicates better corrosion-resistant film on the sample surface (Ref 29). As a result, the corrosion resistance of the passive film on 304 samples decreased first with increasing the strain level below 20% and increased with the strain at a higher strain level, while it increased first with the increase of strain level below 20% and decreased with the strain at a higher strain level for the 316 samples. From the Bode plots, the maximum phase angle values of all samples were  $(-80^\circ) \sim (-90^\circ)$ , revealing the non-idealities of the capacitive property of 304 and 316 steels. The greater the maximum phase angle of the passive film the larger trend of the capacitive property (Ref 30). The sample 304-20% sample had a lower maximum phase angle than that of others (Fig. 5b), while the sample 316-20% displayed a much greater maximum phase angle than that of others (Fig. 5d). Obviously, different capacitance property evolution appeared in the passive films of 304 and 316 steels with

increasing warm pre-strain. Besides, the reaction of passive film leads to the decrease in the phase angle at the low-frequency range, which affects the corrosion resistance of the samples (Ref 31, 32). At the lower frequency range, the phase angle of the sample 304 decreased first with the increase of strain level below 20% and increased with the strain at a higher strain level; the phase angle of the sample 316 increased first with the increase of strain level below 20% and decreased with the strain at a higher strain level. The results suggested that the corrosion reaction of the 304 samples increased first with the increase of strain level below 20% and decreased with the strain at higher strain level, while the corrosion reaction of the 316 samples decreased first as the strain increased below 20% and increased with the strain at a higher strain level.

Some equivalent circuit models were used to interpret the results of EIS tests in stainless steel (Ref 32-34). The EIS results of 304 and 316 steel were fitted using the model in Fig. 5(e). This model considered that the passive films had

capacitive characteristics. A constant phase element (CPE) was introduced to reveal the properties of stainless steel (Ref 35). The CPE is obtained by the following formula (Ref 32):

$$Z(\omega) = Z_0 \cdot (i\omega)^{-n} \quad (\text{Eq 1})$$

$Z_0$  is the proportional factor,  $\omega$  the angular frequency, and  $n$  the CPE exponent. In the equivalent circuit,  $R_s$  represents the electrolyte resistance,  $R_1$  the passive film resistance,  $R_2$  the charge transfer resistance, CPE1 the CPE of the passive film, and CPE2 the CPE of the charge transfer. The fitted results of 304 and 316 samples are displayed in Fig. 5, Tables 4 and 5. Clearly,  $R_1$  and  $R_2$  of 304 samples decreased first with the increase of strain level below 20% and increased with the strain at a higher strain level, but that of 316 samples increased first with the increase of strain level below 20% and decreased with the strain at a higher strain level. Besides, CPE1 and CPE2 of 304 samples increased first with the increase of strain level below 20% and decreased with the strain at a higher strain level, but that of 316 samples decreased first with the increase of strain level below 20% and increased with the strain at a higher strain level. The above results suggested that the corrosion resistance of passive film of 304 steel decreased first with the increase of strain level below 20% and increased with the strain at a higher strain level but that of the 316 steel increased first with the increase of strain level below 20% and decreased with the strain at a higher strain level. The results of the EIS tests are in good agreement with the above polarization tests.

### 3.2 Structural Analysis

The corrosion behavior of stainless steel is generally affected by its structure; thus, the structures of the strained stainless steel should be analyzed. The inverse-pole figure (IPF) results of the EBSD maps for the 304 and 316 steels are displayed in Fig. 6. Both steels exhibited multiple shaped grains and some annealing twins in the unstrained samples. With increasing pre-strain, the grain orientation became more disordered, and the amounts of fine grain clusters increased for both steels. Moreover, the original grain boundaries were interrupted in the 304-50% sample (Fig. 6c), while they were complete and elongated along the rolling direction in the 316-50% sample (Fig. 6f). Much more dislocations accumulated around the grain boundaries in the stainless steels as the strain increased, which could break the grain boundaries or deform the grains.

The intergranular corrosion morphologies of the 304 and 316 steels are shown in Fig. 7. Clearly, the grain boundaries became irregular, and the corrosion extent decreased with increasing strain level for both steels. The original grain boundaries became narrow and were interrupted or even

disappeared when the strain level reached 50%, as shown in the insets of Fig. 7. Moreover, the grain boundaries corrosion of the 316 steel was less severe than that of 304 steel at the same strain level, which was attributed to the addition of Mo in 316 steel (Ref 12). Grain boundaries with the different atomic disorder and free energies exhibit different ion adsorption capabilities in the solution, which will affect the passivation process. This induces the formation of passive films with different characteristics and eventually leads to different corrosion degree between these grain boundaries. Therefore, the intergranular corrosion degree of the warm pre-strained 304 and 316 steels differed significantly, which affected the pitting corrosion behavior.

In addition, the 304 and 316 samples were investigated in XRD tests; the results are displayed in Fig. 8. There were no other diffraction peaks except those of  $\gamma$ -austenite in 304 and 316 steel with or without warm strain. Thus, a warm strain of 304 and 316 steels did not induce phase transformation. In previous studies, Tsay et al. (Ref 36) found that strain-induced martensite formed in the cold strained austenitic stainless steel, while it was not in the stainless steel strained at 150 °C. Besides, Wittig et al. (Ref 37) proposed that phase transformation would not occur in austenitic stainless steel when the strain temperature was higher than 50 °C. The results in this paper were consistent with previous studies. Strain results in adiabatic heating during the higher temperature deformation progress due to the pile-ups of dislocation, and the local overheating could depress the phase transformation. A warm strain of stainless steels helps to overcome some deficiencies of cold strain and has therefore a wide application prospect. Moreover, the intensities of most diffraction peaks slightly decreased with increasing strain level, which may be due to the structural disorder that increased with the strain. Because of the results, the influence of the phase transformation was not considered in the subsequent analysis of the corrosion behavior of the warm-strained stainless steels.

### 3.3 Passive Film Characteristics

The corrosion behavior of stainless steel is associated with the characteristics of the film formed on its surface (Ref 38). Thus, the passive films on the surfaces of the 304 and 316 samples were thoroughly investigated by XPS. The spectra of important components of the films were deconvoluted according to the binding energies after the background subtraction based on the theory of Shirley (Ref 39, 40), and then, the peaks were split into different constituents (Ref 41). The estimations of the possible constituents within the passive films were based on well-characterized standards (Ref 42).

Figure 9 presents the XPS spectra of Fe 2p<sub>3/2</sub>, Cr 2p<sub>3/2</sub>, and O 1s of the passive films on the 304 sample surfaces. The more

**Table 4 Fitted electrochemical parameters of the impedance spectra of the 304 samples with and without warm pre-strain in 3.5 wt.% NaCl solution**

Specimens	$R_s, \Omega\text{cm}^2$	$\text{CPE}_1, \Omega^{-1}\text{cm}^{-2}\text{s}^n$	$n_1$	$R_1, \Omega\text{cm}^2$	$\text{CPE}_2, \Omega^{-1}\text{cm}^{-2}\text{s}^n$	$n_2$	$R_2, \Omega\text{cm}^2$	$\Sigma\chi^2$
304-0%	5.499	$5.384 \times 10^{-5}$	0.914	$2.512 \times 10^4$	$3.202 \times 10^{-4}$	0.909	$9.450 \times 10^3$	$5.631 \times 10^{-4}$
304-10%	5.523	$9.306 \times 10^{-5}$	0.876	$1.551 \times 10^4$	$1.100 \times 10^{-3}$	0.787	$3.936 \times 10^3$	$4.863 \times 10^{-4}$
304-20%	5.346	$9.604 \times 10^{-5}$	0.870	$1.477 \times 10^4$	$1.918 \times 10^{-3}$	0.771	$1.138 \times 10^3$	$4.285 \times 10^{-4}$
304-30%	5.303	$9.101 \times 10^{-5}$	0.901	$1.619 \times 10^4$	$3.747 \times 10^{-4}$	0.827	$4.211 \times 10^3$	$1.813 \times 10^{-3}$
304-50%	5.765	$7.178 \times 10^{-5}$	0.908	$1.676 \times 10^4$	$3.950 \times 10^{-4}$	0.878	$7.841 \times 10^3$	$6.221 \times 10^{-4}$

**Table 5** Fitted electrochemical parameters of the impedance spectra of the 316 samples with and without warm pre-strain in 3.5 wt.% NaCl solution

Specimens	$R_s, \Omega\text{cm}^2$	$\text{CPE}_1, \Omega^{-1}\text{cm}^{-2}\text{s}^n$	$n_1$	$R_1, \Omega\text{cm}^2$	$\text{CPE}_2, \Omega^{-1}\text{cm}^{-2}\text{s}^n$	$n_2$	$R_2, \Omega\text{cm}^2$	$\Sigma\chi^2$
316-0%	5.268	$4.835 \times 10^{-5}$	0.921	$4.269 \times 10^4$	$2.151 \times 10^{-4}$	0.910	$1.541 \times 10^4$	$4.086 \times 10^{-4}$
316-10%	5.674	$3.462 \times 10^{-5}$	0.928	$6.324 \times 10^4$	$1.564 \times 10^{-4}$	0.913	$2.837 \times 10^4$	$1.919 \times 10^{-4}$
316-20%	5.358	$3.027 \times 10^{-5}$	0.932	$7.357 \times 10^4$	$9.235 \times 10^{-5}$	0.926	$4.241 \times 10^4$	$1.378 \times 10^{-4}$
316-30%	5.456	$5.267 \times 10^{-5}$	0.911	$4.145 \times 10^4$	$3.251 \times 10^{-4}$	0.891	$9.687 \times 10^3$	$3.391 \times 10^{-4}$
316-50%	5.135	$6.468 \times 10^{-5}$	0.893	$4.102 \times 10^4$	$5.872 \times 10^{-4}$	0.889	$8.342 \times 10^3$	$2.264 \times 10^{-4}$

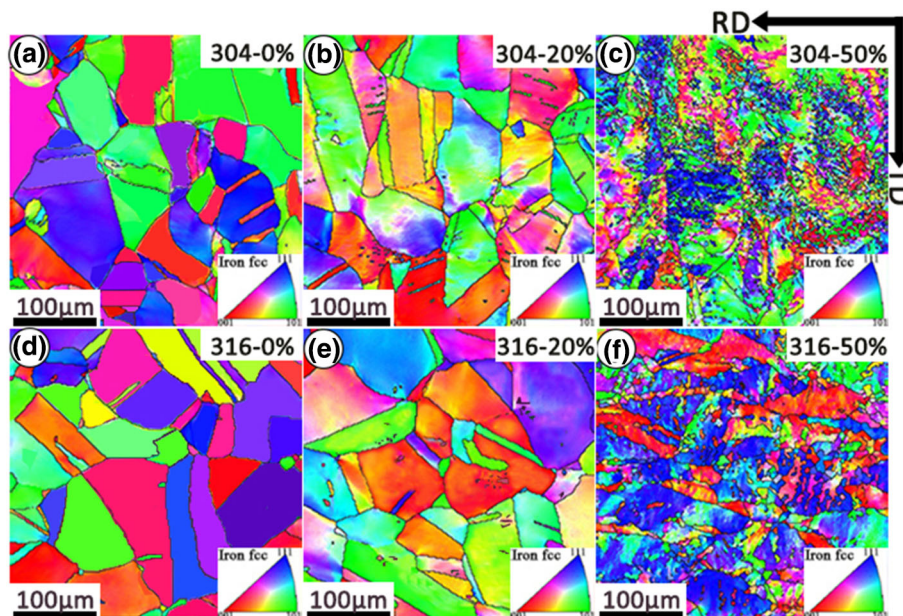


**Fig. 6** EBSD IPF maps of 304 and 316 steels with and without warm pre-strain

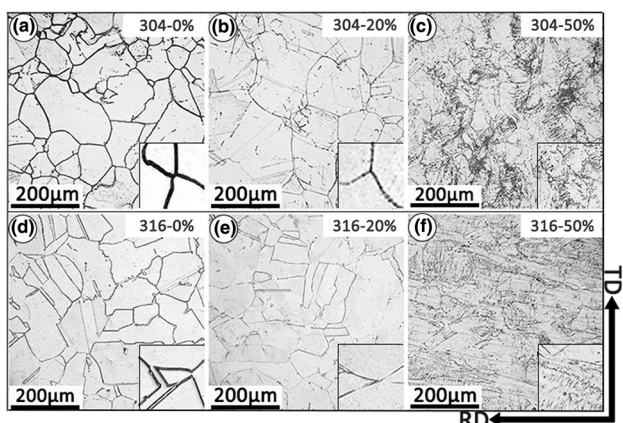


**Fig. 7** Intergranular corrosion morphologies of 304 and 316 steels with and without warm pre-strain

details of the constituents of passive film are presented in Table 6. According to Fig. 9(a1) and (a3), the Fe 2p<sub>3/2</sub> spectrum comprised four constituent peaks at approximately 706.7, 708.2, 709.6, and 711.5 eV, which can be attributed to Fe<sub>met</sub> (the metallic state), Fe<sub>3</sub>O<sub>4</sub>, FeO, and FeOOH species, respectively. Evidently, the intensity of the Fe<sub>met</sub> peak was distinctly higher than those of the Fe<sub>3</sub>O<sub>4</sub>, FeO, and FeOOH

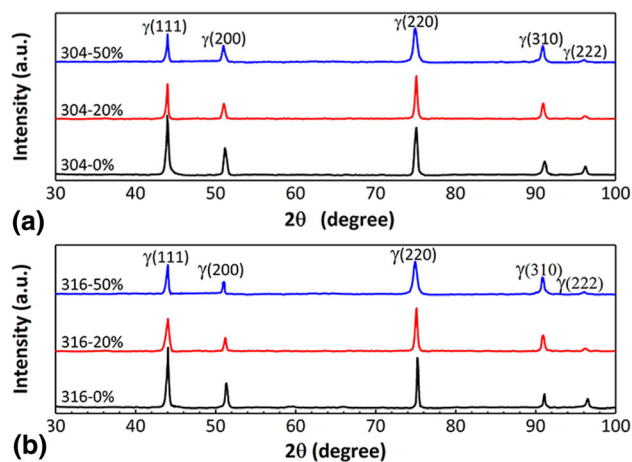


**Fig. 8** XRD plots of 304 and 316 steels with and without warm pre-strain

peaks. The Cr 2p<sub>3/2</sub> spectrum comprised three peaks representing Cr<sub>met</sub> (574.2 eV), Cr<sub>2</sub>O<sub>3</sub> (576.1 eV), and Cr(OH)<sub>3</sub> (577.0 eV) species within the passive films, as shown in Fig. 9(b1) and (b3). Based on the empirical results, the formation of more chromium oxides within the passive film can improve the stabilization of the oxide film and decrease the



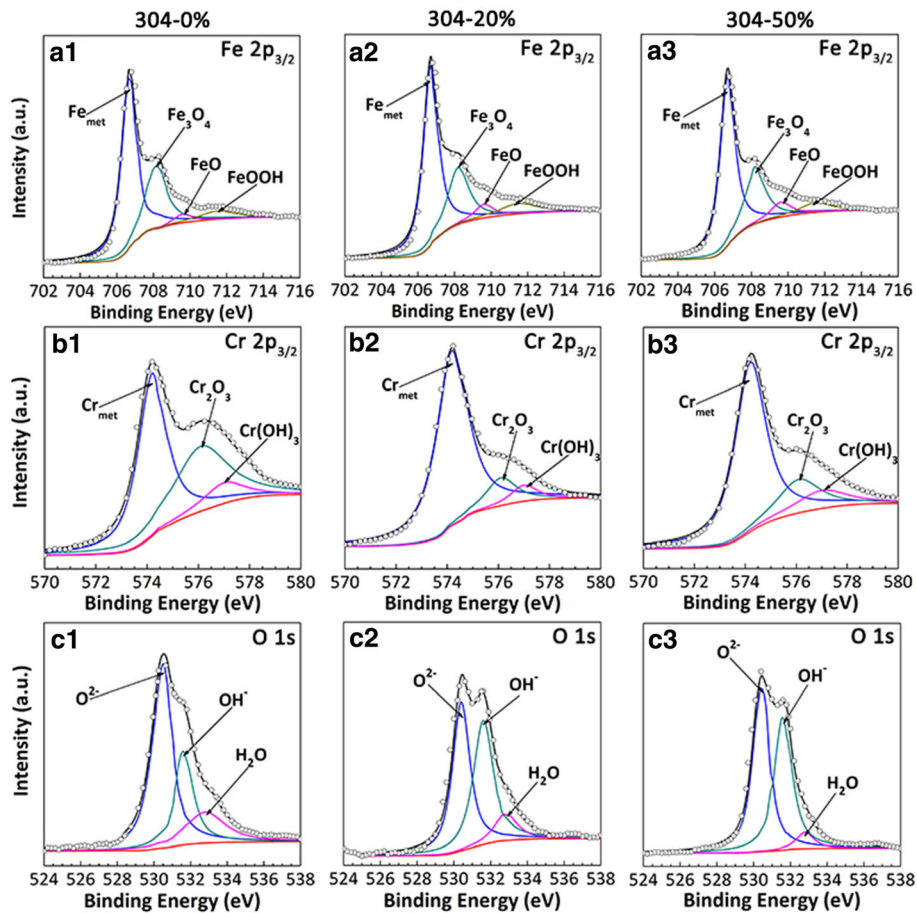


Fig. 9 XPS spectra of the passive film formed on the surfaces of 304 samples. (a1-a3): Fe  $2p_{3/2}$ , (b1-b3): Cr  $2p_{3/2}$ , (c1-c3): O  $1s$

Table 6 XPS analysis of the constituents within the passive film of 304 samples

Element	Compounds	Binding energies, eV	Component proportion, %		
			304-0%	304-20%	304-50%
Fe	FeOOH	711.5	20.01	23.12	23.02
	FeO	709.6	23.64	22.84	23.05
	Fe <sub>3</sub> O <sub>4</sub>	708.2	26.52	25.18	25.24
	Fe <sub>met</sub>	706.7	29.83	28.86	28.69
Cr	Cr(OH) <sub>3</sub>	577.0	29.65	29.78	30.35
	Cr <sub>2</sub> O <sub>3</sub>	576.1	34.14	30.42	32.78
	Cr <sub>met</sub>	574.2	36.21	39.80	36.87
O	H <sub>2</sub> O	533.5	31.38	31.13	33.59
	OH <sup>-</sup>	532.1	32.67	33.68	31.07
	O <sup>2-</sup>	530.4	35.95	35.19	35.34
Cr/Fe			0.18	0.13	0.15

passive current (Ref 43). According to the calculation, the content fraction of the Cr<sub>2</sub>O<sub>3</sub> species within the passive film slightly decreased from 34.14% (304-0%) to 30.42% (304-20%) and then increased to 32.78% (304-50%) with further increasing strain. Moreover, the cationic fraction of the elements in the passive film can be quantitatively evaluated with the following equation (Ref 32):

$$C = \frac{I_m/S_m}{\sum I_n/S_n} \quad (\text{Eq 2})$$

where  $S_m$  represents the sensitivity coefficient and  $I_m$  the superposed intensity of each metallic element peak. The Cr/Fe ratio of the passive film of stainless steel is related to the passivation ability, which further influences the corrosion resistance of stainless steel (Ref 44). Theoretically, the greater the Cr/Fe ratio is, the better the corrosion resistance of the passive film in the corrosive medium is. According to the XPS results of the 304 samples, the Cr/Fe ratios of the passive films of the 304-0%, 304-20%, and 304-50% samples were approx-

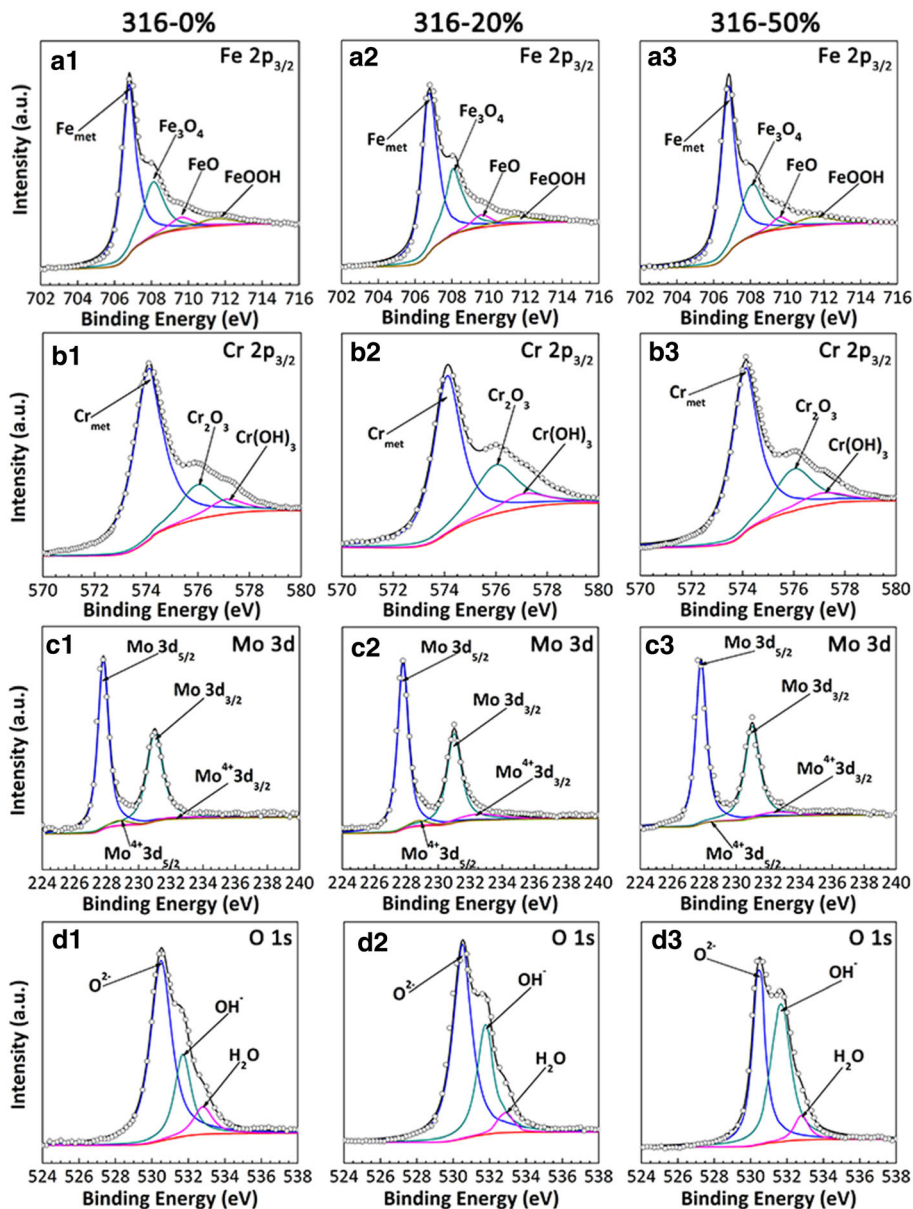


**Fig. 10** XPS spectra of the passive film formed on the surfaces of 316 samples. (a1-a3): Fe  $2p_{3/2}$ , (b1-b3): Cr  $2p_{3/2}$ , (c1-c3): Mo 3d, (d1-d3): O 1s

imately 0.18, 0.13, and 0.15, respectively. Clearly, the Cr/Fe ratio first decreased and then slightly increased with the pre-strain level. That indicates that the passive ability of the pre-strained 304 steel decreased first and then increased with the pre-strain level. In films,  $O^{2-}$  or  $OH^-$  has the function of connecting metal ions. In (Ref 44, 45), it has been proposed that the higher content of the oxide, compared with the hydroxide, within the passive film of stainless steel is beneficial to its corrosion resistance. Accordingly, the O 1s species within the film on the 304 samples were analyzed, and the results are shown in Fig. 9(c1) and (c3). The O 1s spectrum presented the three constituents:  $O^{2-}$  (530.4 eV),  $OH^-$  (532.1 eV), and  $H_2O$  (533.5 eV). Evidently, the intensities of the  $O^{2-}$  peaks (which were associated with  $Cr_2O_3$ ,  $Fe_3O_4$ , and FeO species) were much higher than those of the  $OH^-$  peaks (which were associated with  $Cr(OH)_3$  and FeOOH species). The oxide content of the passive film of the 304 steel decreased

after warm pre-strain, particularly for the steel treated with 20% strain. That may lead to the poor corrosion resistance of sample 304-20%.

Moreover, the passive films formed on the 316 steel surfaces were investigated by XPS; the details of the Fe  $2p_{3/2}$ , Cr  $2p_{3/2}$ , Mo 3d, and O 1s spectra are presented in Fig. 10 and Table 7. The Fe  $2p_{3/2}$  spectrum was associated with the compositions of  $Fe_{met}$  (706.8 eV),  $Fe_3O_4$  (708.1 eV), FeO (709.6 eV), and FeOOH (711.5 eV) species, as shown in Fig. 10(a1) and (a3). The intensity of the  $Fe_{met}$  peak of the 316-20% sample was lower than those of the other samples, and the intensity of the  $Fe_3O_4$  peak slightly changed with increasing pre-strain level. In addition, the Cr  $2p_{3/2}$  spectrum represented three constituents:  $Cr_{met}$  (574.2 eV),  $Cr_2O_3$  (576.1 eV), and  $Cr(OH)_3$  (577.0 eV) (Ref 46, 47). The content of  $Cr_2O_3$  species increased first from 35.67% (316-0%) to 39.19% (316-20%) and then decreased to 38.26% (316-50%), as shown in Fig. 10(b1) and (b3). This

**Table 7 XPS analysis of the constituents within the passive film of 316 samples**

Element	Compounds	Binding energies, eV	Component proportion, %		
			316-0%	316-20%	316-50%
Fe	FeOOH	711.5	22.92	23.30	23.05
	FeO	709.6	25.29	23.83	22.79
	Fe <sub>3</sub> O <sub>4</sub>	708.1	23.01	24.53	25.23
	Fe <sub>met</sub>	706.8	28.78	28.34	28.93
Cr	Cr(OH) <sub>3</sub>	577.0	30.32	28.71	29.85
	Cr <sub>2</sub> O <sub>3</sub>	576.1	35.67	39.19	38.26
	Cr <sub>met</sub>	574.2	34.01	32.10	31.89
Mo	Mo 3d 5/2	227.8	51.34	51.26	51.25
	Mo 3d 3/2	231.0			
	Mo <sup>4+</sup> 3d 5/2	228.8	48.66	48.74	48.75
	Mo <sup>4+</sup> 3d 3/2	232.6			
O	H <sub>2</sub> O	532.8	37.17	29.72	26.98
	OH <sup>-</sup>	531.7	32.25	33.18	37.09
	O <sup>2-</sup>	530.5	30.58	37.10	35.93
Cr/Fe			0.21	0.25	0.22

indicated that the lower warm pre-strain promoted the generation of Cr<sub>2</sub>O<sub>3</sub> within the film of 316 steel in 3.5% NaCl solution, while the higher pre-strain did not. Moreover, the Cr/Fe ratios of samples 316-0%, 316-20%, and 316-50% were approximately 0.21, 0.25, and 0.22, respectively. The Cr/Fe ratios of the passive films on the 316 sample surfaces slightly changed with increasing pre-strain. Evidently, the Cr/Fe ratios of the 316 samples were greater than those of 304 samples. Furthermore, the Mo 3d spectra of the 316 samples are presented in Fig. 10(c1) and (c3). The Mo 3d spectra peaks were deconvoluted into the four constituent peaks Mo 3d<sub>3/2</sub> (231.0 eV), Mo 3d<sub>5/2</sub> (227.8 eV), Mo<sup>4+</sup> 3d<sub>3/2</sub> (232.6 eV), and Mo<sup>4+</sup> 3d<sub>5/2</sub> (228.8 eV). The intensities of Mo 3d<sub>3/2</sub> and Mo 3d<sub>5/2</sub> were similar, while the intensities of the Mo<sup>4+</sup> 3d<sub>5/2</sub> peak slightly decreased with increasing pre-strain. Thus, warm pre-strain affected the Mo constituents within the films on the stainless steel surfaces. Figure 10(d1) and (d3) shows the results of the O1s spectra, which were deconvoluted into several peaks: O<sup>2-</sup> (530.5 eV), OH<sup>-</sup> (531.7 eV), and H<sub>2</sub>O (532.8 eV). The oxide content of the passive film formed on the 316-20% sample surface was greater than those of the other samples. That may lead to the better corrosion resistance of sample 316-20% compared with other samples.

## 4. Discussion

According to the results, warm pre-strain has different effects on the corrosion properties of 304 and 316 steels. Based on the above electrochemical test results, the pitting corrosion resistance of 304 steel decreases with the increase of strain level below 20% and increases with the strain at a higher strain level, while the pitting corrosion resistance of 316 steel increases slightly with the increase of strain level below 20% and decreases with the strain at a higher strain level. Because the macroscopic properties of stainless steel are determined by their components and internal structures, the evolution of the structures induced by warm pre-strain in 304 and 316 steels should be thoroughly investigated to clarify their abnormal

corrosion behavior. The effect of structures on the corrosion behavior will be discussed in more detail in the next section.

### 4.1 Effect of Inclusions and Pores on Pitting Corrosion Behavior

Inclusions and pores were generally unavoidable in stainless steel due to the forming process. Inclusions in stainless steel will lead to the depletion of Cr in the surrounding materials, resulting in pitting corrosion initiates more easily at inclusions (Ref 48). In general, inclusions form easily at the grain boundaries of stainless steel, which are very susceptible to corrosion (Ref 49). However, several researchers (Ref 50, 51) have demonstrated that some inclusions in stainless steel may not trigger pitting corrosion, which depends on the chemical composition, size, and shape of the inclusions. Furthermore, inclusions dissolve after pitting corrosion (Ref 52), thereby making it difficult to determine whether the pitting corrosion occurs preferentially at inclusions. Pores are another important factor that affects the corrosion behavior of stainless steel; nevertheless, the porosity of stainless steel can be decreased by improving the machining process (Ref 53). Sun et al. (Ref 54) reported that pitting initiation is more likely to occur in the pores of stainless steel when its porosity is greater than 1%.

To investigate the inclusions or pores in the 304 and 316 steels, the surface morphologies of the polished 304 and 316 steels without deformations were repeatedly studied with a metallographic microscope. The surface morphologies of the polished stainless steels and the SEM-EDS tests results of the inclusions in the steels are shown in Fig. 11. Clearly, only a few inclusions and almost no big pores were found in both steels (Fig. 11a and b); the EDS tests revealed the MnS inclusions in both steel (Fig. 11c and d). The investigated stainless steels exhibited few inclusions, a small part of which could be attacked by pitting corrosion. However, it was discovered that the corrosion pits preferentially formed at the grain boundaries (as shown in Fig. 3) in both steel types during the potentiodynamic polarization tests. Therefore, it is reasonable to assume that pitting corrosion is more likely to occur at inclusions on grain boundaries. Meanwhile, a small number of pores have little influence on the corrosion behavior of stainless steels.

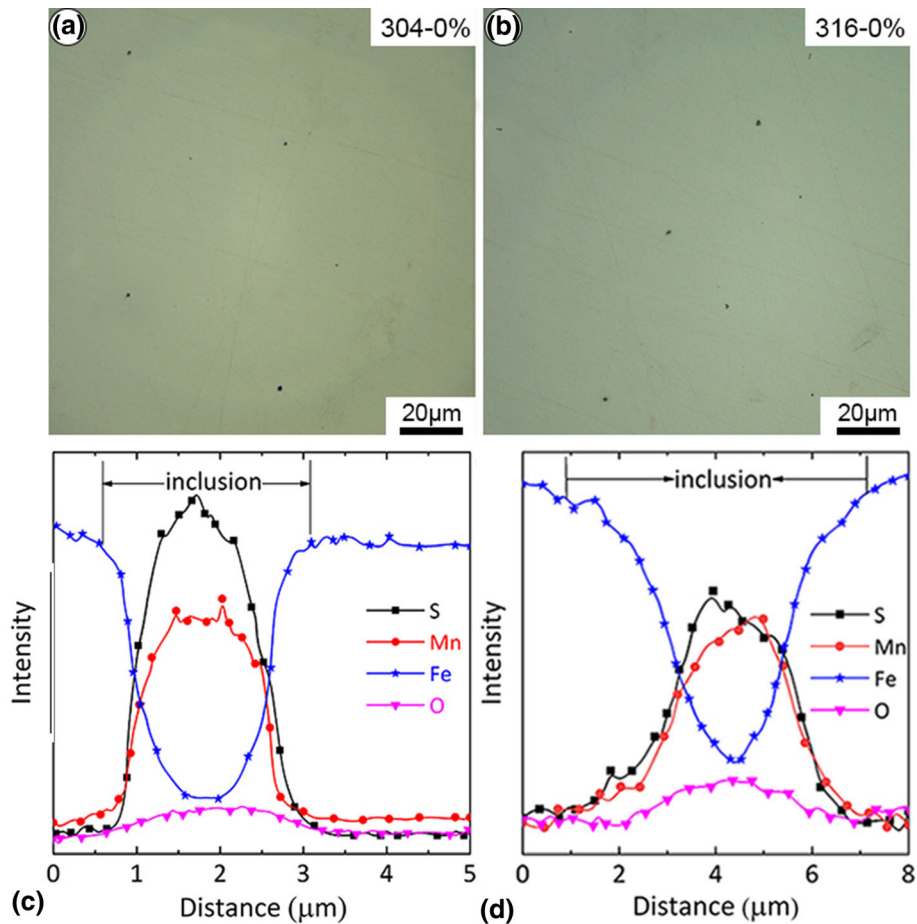


**Fig. 11** (a, b): Surface morphologies of 304 and 316 steels after polishing; (c, d): SEM-EDS tests of the inclusions in both steels

Thus, the effects of the inclusions and pores on the abnormal corrosion behavior of the 304 and 316 steels were not further investigated. Some researchers (Ref 25, 55) have revealed that the structure of stainless steel strongly affects its corrosion behavior. In this work, the structures of warm-strained 304 and 316 steels were significantly affected by different strain levels, which may have caused the different corrosion behavior. The structures of warm-strained stainless steels should be thoroughly investigated to analyze the evolution of the corrosion behavior.

#### 4.2 Effect of Grain Size Distribution on Pitting Corrosion Behavior

Some researchers have reported that grain refinement of stainless steel can improve the corrosion resistance (Ref 56); however, it has also been stated that the corrosion behavior of stainless steel is not influenced by the grain size (Ref 57). How the grain size affects the pitting corrosion behavior of materials has always been controversial, and no clear explanation has also been provided. The grain size of the crystal can be effectively analyzed by the EBSD according to the orientation of many points (Ref 58). Previous structural analysis in Fig. 5 displayed that the grains of 304 and 316 steels were obviously changed by large strain, while small strain did not. Figure 12 shows the average grain diameters of the warm pre-strained 304 and 316 samples based on the EBSD tests. Most grains in the 304 and 316 steels at 20% strain had diameters of 90–110 μm

(Fig. 12a and c), while most grain diameters were below 30 μm for the samples at 50% strain (Fig. 12b and d). According to the calculation, the average grain size distinctly decreased with increasing pre-strain in both steels, and the grain size of sample 316-50% was greater than that of sample 304-50%, as shown in Fig. 12e. The decreased grain size of the sample at 50% strain was attributed to the formation of many fine grains. Moreover, the original grain boundaries in the 304-50% sample were severely interrupted, while those in the 316-50% sample were not (Fig. 2c and f). This resulted in a greater grain size in the 316-50% sample compared with that of the 304-50% sample. In this study, the grain size of both 304 and 316 steels decreased with increasing pre-strain, while their pitting corrosion behavior evolutions were different. Thus, there is no definite correlation between grain size and corrosion behavior. The grains of the material were divided by grain boundaries; thus, the grain sizes of the materials were determined by the grain boundary distribution. The changes in the grain boundary distribution in the warm pre-strained 304 and 316 steels are analyzed in detail in the next section.

#### 4.3 Effect of Grain Boundaries Distribution on Pitting Corrosion Behavior

Grain boundaries, which are vital crystal defects, have a chaotic atomic arrangement and higher free interfacial energies than the matrix. This stimulates ion chemisorption and induces pitting corrosion (Ref 51). According to the structural analysis

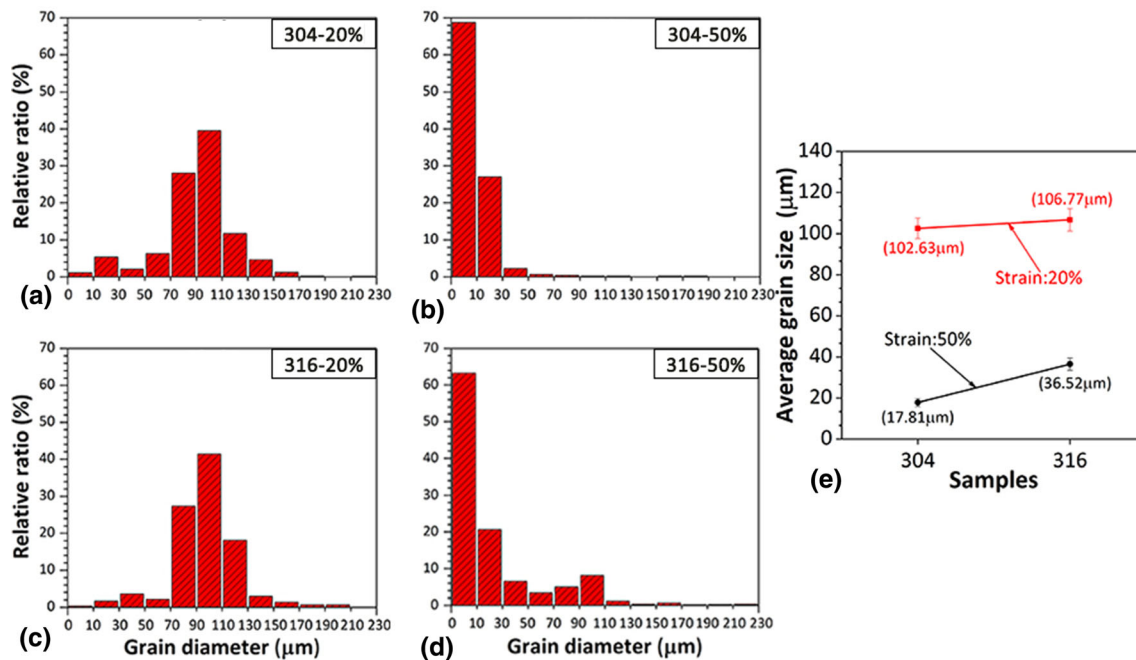


**Fig. 12** Statistics of grain size of warm pre-strained 304 and 316 steels. (a-d): relative ratio of grain distribution with different size ranges. (e): average grain size of warm pre-strained 304 and 316 steels

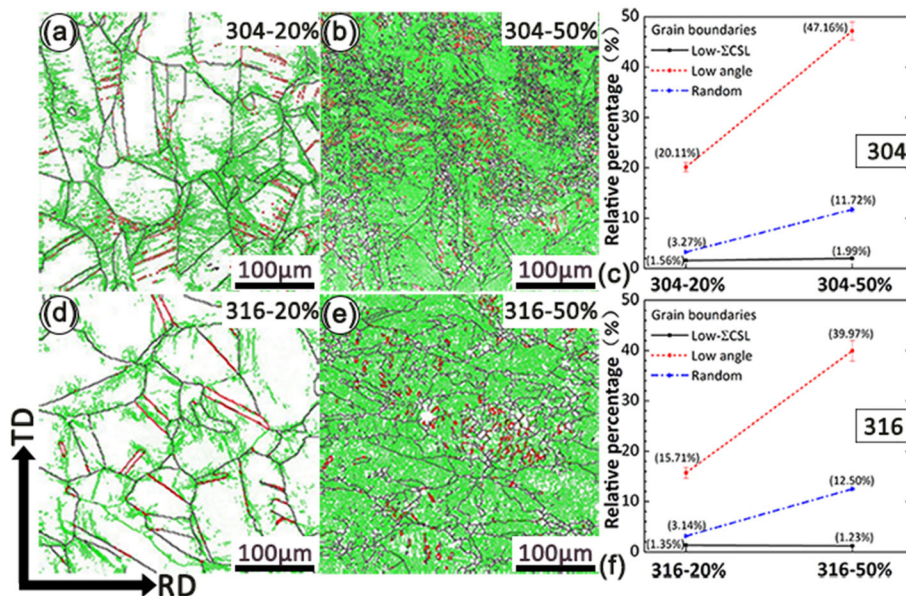


**Fig. 13** (a–e): Grain boundaries distributions of warm pre-strained 304 and 316 steels. (c, f): Statistics of grain boundaries content of warm pre-strained 304 and 316 steels. Black, green, and red lines represent the random, low angle, and low-ΣCSL grain boundaries, respectively (Color figure online)

in Fig. 7, the grain boundaries of 304 and 316 steels were obviously changed by warm pre-strain; so, studying the evolution of the corrosion behavior of warm pre-strained stainless steel by analyzing the grain boundary distribution is crucial. Figure 13 shows the grain boundary distributions of the warm pre-strained 304 and 316 steels. The grain boundaries can be categorized into high angle or low angle grain boundaries (LAGBs) according to the orientation difference (over or below

15°, respectively). Regarding the coincidence site lattice boundaries, those with  $\Sigma \leq 29$  are categorized as the low- $\Sigma$  coincidence site lattice grain boundaries (low- $\Sigma$ CSLGBs) (Ref 59, 60). In this paper, the LAGBs and low- $\Sigma$ CSLGBs are represented by green and red lines, respectively; the remaining grain boundaries are categorized as random grain boundaries (RGBs), which are represented by black lines. Grain boundaries are defects that can be sensitive to corrosion depending on their

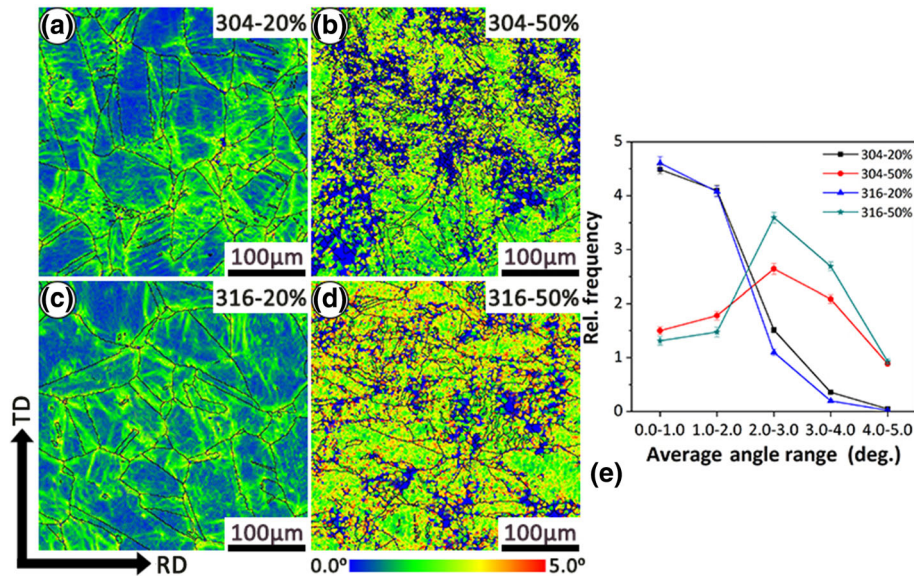


**Fig. 14** (a-d): EBSD maps of local misorientation of warm pre-strained 304 and 316 steels. (e): Statistics of the relative frequency of local misorientation in the average angle range of 0.0-5.0 degrees

crystallographic nature and atomic structures (Ref 61-63). The low- $\Sigma$ CSLGBs possess a highly regular atomic structure and very low energy; thus, they are sufficiently immune to corrosion (Ref 64, 65). Hence, the corrosion properties of steels are little influenced by low- $\Sigma$ CSLGBs. The LAGBs have lower energies compared with those of RGBs owing to the lower degree of misorientation, which leads to a higher immunity to corrosion (Ref 66). Furthermore, the corrosion resistance of the grain boundaries of the 316 steel is much better than that of the 304 steel owing to the alloying element Mo (Fig. 7). The differences in the corrosion resistance of the grain boundaries will further affect the pitting corrosion behavior of stainless steel because of the preferential occurrence of corrosion at grain boundaries. The original RGB shapes of the steels at a lower strain were retained, while their structures changed, and the grain boundary distribution distinctly changed for the steels at a higher strain (Fig. 13c and f). Evidently, the RGBs became narrower and more chaotic with increasing strain levels. As the strain reached 50%, the original RGBs were severely interrupted in the 304 steel (Fig. 13c), whereas this was not the case for those in the 316 steel (Fig. 13f). The RGBs of stainless steels can result in higher corrosion susceptibility. As a result, the corrosion susceptibility of the 304 steel sharply decreased compared with that of the 316 steel at 50% strain owing to the severely interrupted RGBs. In addition, LAGBs accumulated around the original RGBs of samples at 20% strain (Fig. 13a and d), whereas they covered approximately the entire sample at 50% strain (Fig. 13b and e). The LAGBs content was higher in 304 steel than in 316 steel at equal strain, and the LAGBs increased the corrosion susceptibility of both steels with increasing strain level.

#### 4.4 Effect of Dislocations Evolution on Pitting Corrosion Behavior

According to the previous study (Ref 67, 68), the dislocations also affect the corrosion behavior of stainless steels. In general, the geometrically necessary dislocations (GNDs) of strained material can be extrapolated with the theory of Gao and Kubin (Ref 69, 70):

$$\beta_{GND} = \frac{2\alpha}{ub} \quad (\text{Eq 3})$$

where  $\beta_{GND}$  is the GND density,  $\alpha$  the local misorientation,  $u$  the step length (1.5  $\mu\text{m}$ ) of the local misorientation, and  $b$  the Burgers vector (0.125 for ferrite). Evidently, the local misorientation angle is proportional to the  $\beta_{GND}$ , which determines the dislocation of the sample. The results of the local misorientation from the EBSD data of the strained 304 and 316 samples are displayed in Fig. 14. According to the calculation, the  $\beta_{GND}$  of samples 304-20%, 304-50%, 316-20%, and 316-50% were approximately  $2.787 \times 10^{-4} \text{ nm}^{-2}$ ,  $3.840 \times 10^{-4} \text{ nm}^{-2}$ ,  $2.540 \times 10^{-4} \text{ nm}^{-2}$ , and  $4.480 \times 10^{-4} \text{ nm}^{-2}$ , respectively. Thus, the  $\beta_{GND}$  increased with the strain level in both steels, and the  $\beta_{GND}$  was similar in both steels at 20% strain, whereas it was lower in the 304 steel than in the 316 steel at 50% strain. The different  $\beta_{GND}$  values between the 304 and 316 steels were caused by their different essential characteristics. To determine the reason, the nano-hardness distributions of the 304 and 316 steels before the strain were determined with the Agilent G200 nano-indenter. A total of  $30 \times 30$  indentation points were created on the samples with a maximal load of 1 mN (Fig. 15a). According to the results, the

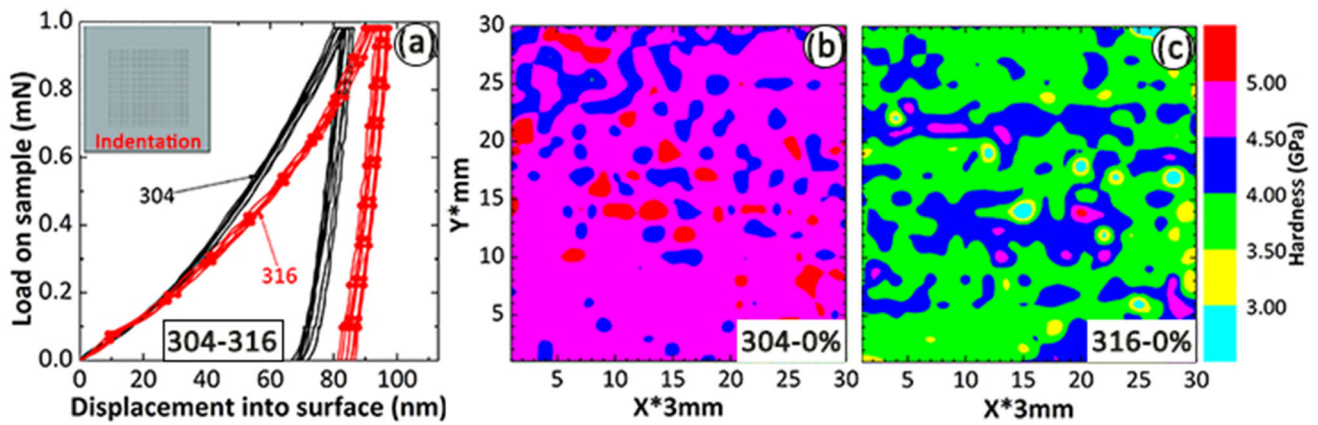


**Fig. 15** (a): Typical load versus displacement curves of 304 and 316 steels. (b, c): Contour plots of the nano-hardness distribution of unstrained 304 and 316 steels. The indentations on the samples were displayed in the inset of Fig. 15(a)

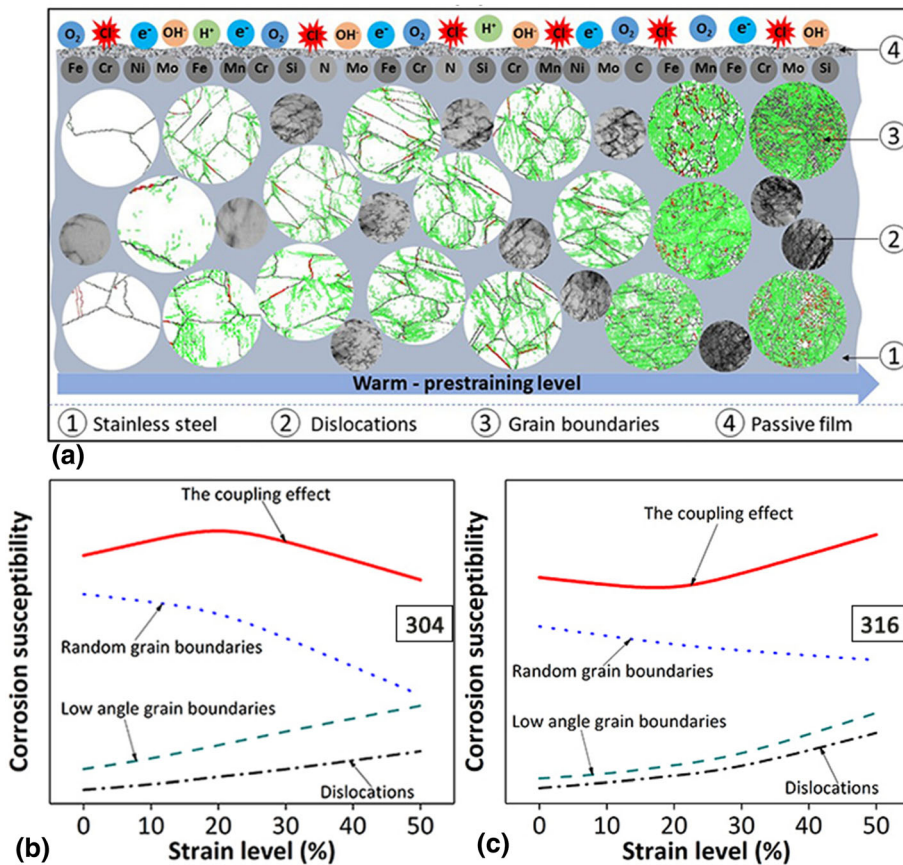


**Fig. 16** Schematic illustration of the coupling effect of the grain boundaries and microstructures on the corrosion susceptibility of the warm pre-strained 304 and 316 steels

nano-hardness of the 304 steel (Fig. 15b) was much higher than that of the 316 steel (Fig. 15c) before the strain. In general, the hardness of stainless steel has a great influence on its strain process. The 304 steel was difficult to deform owing to its higher nano-hardness; consequently, its grains were broken during the high strain process. By contrast, the 316 steel was easily deformable during the high strain process owing to its lower nano-hardness, which resulted in the formation of uninterrupted grains and more dislocations. Furthermore,

different stacking fault energies (SFE) of the 304 and 316 steels may induce various dislocation–dislocation interactions associated with different slip systems under strain (Ref 71–73). A low SFE of stainless steel facilitates the segregation of dislocations and the occurrence of stacking faults, which can promote the twinning process. All these properties resulted in the different dislocation density of the 304 and 316 steels during the straining process. Dislocation enrichment regions of stainless steels were easy to induce corrosion, especially pitting

corrosion (Ref 67, 68). Thus, more dislocations in stainless steels can result in higher corrosion susceptibility. As a result, the corrosion susceptibility of the dislocations increased with the strain level in both steels; the strain levels were similar in both steels at 20% strain, whereas that of the 304 steel was lower than that of the 316 steel at 50% strain.

#### 4.5 Coupling Effect of Grain Boundaries and Microstructure on Pitting Corrosion Behavior

According to the previous analysis, warm pre-strain significantly changed the structures of the 304 and 316 steels. For the 304 steel, the dislocations and LGBs became significantly more dominant at a low pre-strain (20%), and the RGBs were interrupted at the higher pre-strain (50%). However, for the 316 steel, the dominant RGBs were not interrupted during warm pre-strain, and the dislocations and LAGBs significantly increased at the higher strain (50%). The coupling effect of above chaotic structures in stainless steel increased the atomic disorder and free energy. That changes the adsorption process of ions in the medium, thus affecting the passive film characteristics. The Cr/Fe ratio of the passive film of the 316 steel was higher than that of the 304 steel. The oxide content of the passive film of the 304 steel at 20% strain was lower and that of the 316 steel was higher. Then, the oxide films on the steel surface influenced the corrosion behavior, as described in Fig. 16(a). Figure 16(b) and (c) present the effect of the coupled grain boundaries and microstructures on the corrosion susceptibility of the warm pre-strained 304 and 316 steels, respectively. As a result, the pitting corrosion susceptibility of the 304 steel increased with the increase of strain level below 20% and decreased with the strain at a higher strain level, while the pitting corrosion resistance of 316 steel increases slightly with the increase of strain level below 20% and decreases with the strain at a higher strain level. Knowing the corrosion mechanism enables the design of advanced stainless steel with high strength and corrosion resistance. The results presented in this work are of value for academic research and industrial applications.

## 5. Conclusions

The effect of warm pre-strain on the pitting corrosion of the 304 and 316 steels in 3.5% NaCl solution was studied by using electrochemical tests, passive film characterization, and structural analysis. The following conclusions can be drawn:

1. The pitting corrosion resistance of 304 steel decreased with the increase of strain level below 20% and increases with the strain at a higher strain level, while the pitting corrosion resistance of 316 steel increases slightly with the increase of strain level below 20% and decreases with the strain at a higher strain level.
2. The random grain boundaries in 304 steel are interrupted with the increase of strain level higher than 20%; this does not occur in 316 steel, which exhibits more dislocations. The interrupted random grain boundaries decreased the pitting corrosion susceptibility, while more dislocation increased it.
3. The coupling effect of microstructures induced by warm pre-strain affected the oxide content of the passive film,

especially for the chromium oxide, which results in abnormal corrosion behavior.

## Acknowledgments

This research was supported by the National Key Research and Development Program of China (2019YFB150530202), the National Natural Science Foundation of China (51971204), and the Zhejiang Provincial Natural Science Foundation of China (LY19E010006).

## References

1. Y.M. Wang, T. Voisin, J.T. Mckeown, J. Ye, and T. Zhu, Additively Manufactured Hierarchical Stainless Steels with High Strength and Ductility, *Nat. Mater.*, 2017, **17**, p 63–71
2. R. Casati, J. Lemke, and M. Vedani, Microstructure and Fracture Behavior of 316L Austenitic Stainless Steel Produced by Selective Laser Melting, *J. Mater. Sci. Technol.*, 2016, **32**, p 738–744
3. M. Terada, R.A. Antunes, A.F. Padilha, and I. Costa, Corrosion Resistance of Three Austenitic Stainless Steels for Biomedical Applications, *Mater. Corros.*, 2007, **58**, p 762–766
4. M. Michiuchi, H. Kokawa, Z.J. Wang, Y.S. Sato, and K. Sakai, Twin-induced Grain Boundary Engineering for 316 Austenitic Stainless Steel, *Acta Mater.*, 2006, **54**, p 5179–5184
5. M.A.M. Ibrahim, S.S.A.E. Rehim, and M.M. Hamza, Corrosion Behavior of Some Austenitic Stainless Steels in Chloride Environments, *Mater. Chem. Phys.*, 2009, **115**, p 80–85
6. S. Ningshen, U.K. Mudali, G. Amarendra, and R. Baldev, Corrosion Assessment of Nitric Acid Grade Austenitic Stainless Steels, *Corros. Sci.*, 2009, **51**, p 322–329
7. A. Pardo, M.C. Merino, A.E. Coy, F. Viejo, R. Arrabal, and E. Matykina, Pitting Corrosion Behaviour of Austenitic Stainless Steels-Combining Effects of Mn and Mo Additions, *Corros. Sci.*, 2008, **50**, p 1796–1806
8. A. Belyakov, M. Odnobokova, I. Shakhova, and R. Kaibyshev, Regularities of Microstructure Evolution and Strengthening Mechanisms of Austenitic Stainless Steels Subjected to Large Strain Cold Working, *Mater. Sci. Forum*, 2016, **879**, p 224–229
9. S. Azuma, T. Kudo, H. Miyuki, M. Yamashita, and H. Uchida, Effect of Nickel Alloying on Crevice Corrosion Resistance of Stainless Steels, *Corros. Sci.*, 2004, **46**, p 2265–2280
10. M.A. Ameer, A.M. Fekry, and E.T. Heikal, Electrochemical Behaviour of Passive Films on Molybdenum-containing Austenitic Stainless Steels in Aqueous Solutions, *Electrochim. Acta*, 2005, **50**, p 43–49
11. A. Belfrouh, C. Masson, D. Vouagner, A.M.D. Beccdelievre, N.S. Prakash, and J.P. Audouard, The Cumulative Effect of Alloying Elements N, W, Mo and Cu on the Corrosion Behaviour of 17Cr-13Ni Stainless Steel in 2NH<sub>2</sub>SO<sub>4</sub>, *Corros. Sci.*, 1996, **38**, p 1639–1648
12. X.Y. Li and K. Lu, Improving Sustainability with Simpler Alloys, *Science*, 2019, **364**, p 733–734
13. L. Peguet, B. Malki, and B. Baroux, Influence of Cold Working on the Pitting Corrosion Resistance of Stainless Steels, *Corros. Sci.*, 2007, **49**, p 1933–1948
14. M. Hadji and R. Badji, Microstructure and Mechanical Properties of Austenitic Stainless Steels after Cold Rolling, *J. Mater. Eng. Perform.*, 2002, **11**, p 145–151
15. P. Cizek, J.A. Whiteman, W.M. Rainforth, and J.H. Beynon, EBSD and TEM Investigation of the Hot Deformation Substructure Characteristics of a Type 316L Austenitic Stainless Steel, *J. Microsc.*, 2004, **213**, p 285–295
16. M. Eskandari, A. Zarei-Hanzaki, and H.R. Abedi, An Investigation into the Room Temperature Mechanical Properties of Nanocrystalline Austenitic Stainless Steels, *Mater. Design*, 2014, **45**, p 674–681
17. H.M. Tao, C.S. Zhou, Y.Y. Zheng, Y.J. Hong, J.Y. Zheng, and L. Zhang, Anomalous Evolution of Corrosion Behaviour of Warm-rolled



- Type 304 Austenitic Stainless Steel, *Corros. Sci.*, 2019, **154**, p 268–276
18. X.Y. Chen, L.L. Ma, C.S. Zhou, Y.J. Hong, H.M. Tao, J.Y. Zheng, and L. Zhang, Improved Resistance to Hydrogen Environment Embrittlement of Warm Deformed 304 Austenitic Stainless Steel in High-pressure Hydrogen Atmosphere, *Corros. Sci.*, 2019, **148**, p 159–170
  19. J.O. Nilsson, P. Kangas, A. Wilson, and T. Karlsson, Mechanical Properties, Microstructural Stability and Kinetics of  $\Sigma$ -Phase Formation in 29Cr-6Ni-2Mo-0.38 N Superduplex Stainless Steel, *Metall. Mater. Trans. A* 2000, **31**, p 35–45
  20. M.A. Gebril, M.S. Aldemey, F.I. Haider, and N. Ali, Effect of Austenizing and Tempering Time on Corrosion Rate of Austenitic Stainless Steel in Oxalic Acid, *Adv. Mater. Res.*, 2014, **980**, p 46–51
  21. Q. Zhou, S. Ping, X. Meng, R. Wang, and Y. Gao, Precipitation Kinetics of  $M_{23}C_6$  Carbides in the Super 304H Austenitic Heat-Resistant Steel, *J. Mater. Eng. Perform.*, 2017, **26**, p 6130–6139
  22. W. Xu, N. Birbilis, G. Sha, Y. Wang, J.E. Daniels, Y. Xiao, and M. Ferry, A High-Specific-Strength and Corrosion-Resistant Magnesium Alloy, *Nat. Mater.*, 2015, **14**, p 1229–1235
  23. R.D. Moser, P.M. Singh, L.F. Kahn, and K.E. Kurtis, Chloride-induced Corrosion Resistance of High-Strength Stainless Steels in Simulated Alkaline and Carbonated Concrete Pore Solutions, *Corros. Sci.*, 2012, **57**, p 241–253
  24. E.E. Oguzie, J. Li, Y. Liu, D. Chen, L. Ying, Y. Ke, and F.H. Wang, The Effect of Cu Addition on the Electrochemical Corrosion and Passivation Behavior of Stainless Steels, *Electrochim. Acta*, 2010, **55**, p 5028–5035
  25. X.D. Chen, Y.S. Li, Y.T. Zhu, Y.K. Bai, and B. Yang, Improved Corrosion Resistance of 316LN Stainless Steel Performed by Rotationally Accelerated Shot Peening, *Appl. Surf. Sci.*, 2019, **481**, p 1305–1312
  26. J.H. Liu, E.A. Han, Y.W. Song, and D.Y. Shan, Effect of Twins on the Corrosion Behavior of Mg-5Y-7Gd-1Nd-0.5Zr Mg Alloy, *J. Alloys Compd.* 2018, **757**, p 356–363
  27. L. Guan, B. Zhang, X.P. Yong, J.Q. Wang, E.H. Han, and W. Ke, Effects of Cyclic Stress on the Metastable Pitting Characteristic for 304 Stainless Steel under Potentiostatic Polarization, *Corros. Sci.*, 2015, **93**, p 80–89
  28. G. Burstein, P. Pistorius, and S. Mattin, The Nucleation and Growth of Corrosion Pits on Stainless Steel, *Corros. Sci.*, 1993, **35**, p 57–62
  29. C.N. Cao, On The Impedance Plane Displays for Irreversible Electrode Reactions Based on the Stability Conditions of the Steady-state-II. One State Variable Besides Electrode Potential, *Electrochim. Acta*, 1990, **35**, p 831–836
  30. T. Balusamy, M. Jamesh, S. Kumar, and T.S.N. Sankara Narayanan, Corrosion Resistant Ti Alloy for Sulphuric Acid Medium: Suitability of Ti-Mo Alloys, *Mater. Corros.*, 2012, **63**, p 803–806
  31. S.L.D. Assis, S. Wolynec, and I. Costa, Corrosion Characterization of Titanium Alloys by Electrochemical Techniques, *Electrochim. Acta*, 2006, **51**, p 1815–1819
  32. H. Luo, X.Z. Wang, C.F. Dong, K. Xiao, and X.G. Li, Effect of Cold Deformation on the Corrosion Behavior of UNS31803 Duplex Stainless Steel in Simulated Concrete Pore Solution, *Corros. Sci.*, 2017, **178**, p 178–192
  33. E. Hug, R.P. Babu, I. Monnet, A. Etienne, F. Moisy, V. Pralong, N. Enikeev, M. Abramova, X. Sauvage, and B. Radiguet, Impact of the Nanostructuring on the Corrosion Resistance and Hardness of Irradiated 316 Austenitic Stainless Steels, *Appl. Surf. Sci.*, 2017, **1026**, p 1026–1035
  34. G. Blustein, R. Romagnoli, J.A. Jaen, A.R. Di Sarli, and B. del Amo, Aluminum Basic Benzoate-Based Coatings: Evaluation of Anticorrosion Properties by Electrochemical Impedance Spectroscopy and Accelerated Tests, *Corrosion*, 2007, **63**, p 899–915
  35. D. Nakhaie, I. Taji, M.H. Moayed, and E. Asselin, Dependence of the Electrochemical and Passive Behavior of the Lead-Acid Battery Positive Grid On Electrode Surface Roughness, *Corrosion*, 2017, **73**, p 1359–1366
  36. L.W. Tsay, Y.J. Lin, and C. Chen, The Effect of Rolling Temperature and Sensitization Treatment on the Surface Corrosion Cracking of 304L Stainless Steel, *Corros. Sci.*, 2012, **63**, p 267–274
  37. J.E. Wittig, M. Pozuelo, J.A. Jiménez, and G. Frommeyer, Temperature Dependent Deformation Mechanisms of a High Nitrogen-Manganese Austenitic Stainless Steel, *Steel Res. Int.*, 2009, **80**, p 66–70
  38. H. Luo, X.Z. Wang, C.F. Dong, K. Xiao, and X.G. Li, Effect of Cold Deformation on the Corrosion Behaviour of UNS S31803 Duplex Stainless Steel in Simulated Concrete Pore Solution, *Corros. Sci.*, 2017, **124**, p 178–192
  39. C.T. Liu and J.K. Wu, Influence of pH on the Passivation Behavior of 254SMO Stainless Steel in 3.5% NaCl Solution, *Corros. Sci.*, 2007, **49**, p 2198–2209
  40. D.A. Shirley, High-resolution x-ray Photoemission Spectrum of the Valence Bands of Gold, *Phys. Rev. B*, 1972, **5**, p 4709–4714
  41. S. Haupt, C. Calinski, U. Collisi, H.W. Hoppe, D. Speckmann, and H.H.S. Strehlow, XPS and ISS Examinations of Electrode Surface and Passive Layers with a Specimen Transfer in a Closed System, *Surf. Interf. Anal.*, 1986, **9**, p 357–365
  42. Z.C. Feng, X.Q. Cheng, C.F. Dong, L. Xu, and X.G. Li, Passivity of 316L Stainless Steel in Borate Buffer Solution Studied by Mott-Schottky Analysis, Atomic Absorption Spectrometry and x-Ray Photoelectron Spectroscopy, *Corros. Sci.*, 2010, **52**, p 3646–3653
  43. S.V. Phadnis, A.K. Satpati, K.P. Muthe, J.C. Vyas, and R.I. Sundaresan, Comparison of Rolled and Heat Treated SS304 in Chloride Solution Using Electrochemical and XPS Techniques, *Corros. Sci.*, 2003, **45**, p 2467–2483
  44. H. Luo, H.Z. Su, G.B. Ying, C.F. Dong, and X.G. Li, Effect of Cold Deformation on the Electrochemical Behaviour of 304L Stainless Steel in Contaminated Sulfuric Acid Environment, *Appl. Surf. Sci.*, 2017, **425**, p 628–638
  45. W. Fredriksson, D. Petrini, K. Edstrom, F. Bjorefors, and L. Nyholm, Corrosion Resistances and Passivation of Powder Metallurgical and Conventionally Cast 316L and 2205 Stainless Steels, *Corros. Sci.*, 2013, **67**, p 268–280
  46. I. Nacic and D.D. Macdonald, The Passivity of Type 316 l Stainless Steel in Borate Buffer Solution, *J. Nucl. Mater.*, 2008, **379**, p 54–58
  47. Z.Y. Cui, L.W. Wang, H.T. Ni, W.K. Hao, C. Man, S.S. Chen, X. Wang, Z.Y. Liu, and X.G. Li, Influence of Temperature on the Electrochemical and Passivation Behavior of 2507 Super Duplex Stainless Steel in Simulated Desulfurized Flue Gas Condensates, *Corros. Sci.*, 2017, **118**, p 31–48
  48. K. Saeidi, X. Gao, and Y. Zhong, Hardened Austenite Steel with Columnar Sub-Grain Structure Formed by Laser Melting, *Mater. Sci. Eng., A*, 2015, **625**, p 221–229
  49. Q. Liu, S.F. Yang, M.J. Zhao, L.B. Zhu, and J.S. Li, Pitting Corrosion of Steel Induced by Al<sub>2</sub>O<sub>3</sub> Inclusions, *Metals*, 2017, **7**, p 347
  50. A. Chiba, I. Muto, and Y. Sugawara, Effect of Inclusion Size on Pit Initiation at Mns in Stainless Steel, ECS & SMEQ Joint International Meeting, 2014
  51. P. Schmuki, H. Hildebrand, A. Friedrich, and S. Virtanen, The Composition of the Boundary Region of Mns Inclusions in Stainless Steel and Its Relevance in Triggering Pitting Corrosion, *Corros. Sci.*, 2005, **47**, p 1239–1250
  52. B. Zhang, J. Wang, B. Wu, Y.T. Zhou, and X.L. Ma, Quasi-in situ Ex-Polarized TEM Observation on Dissolution of Mns Inclusions and Metastable Pitting of Austenitic Stainless Steel, *Corros. Sci.*, 2015, **100**, p 295–305
  53. C. Man, C.F. Dong, and T.T. Liu, The Enhancement of Microstructure on the Passive and Pitting Behaviors of Selective Laser Melting 316L SS in Simulated Body Fluid, *Appl. Surf. Sci.*, 2019, **467**, p 193–205
  54. Z.J. Sun, X.P. Tan, S.B. Tor, and W.Y. Teong, Selective Laser Melting of Stainless Steel 316L with Low Porosity and High Build Rates, *Mater. Des.*, 2016, **104**, p 197–204
  55. Q.H. Wang, B.H. Zhang, Y.B. Ren, and K. Yang, Eliminating Detrimental Effect of Cold Working on Pitting Corrosion Resistance in High Nitrogen Austenitic Stainless Steels, *Corros. Sci.*, 2017, **123**, p 351–355
  56. J.L. Lv, H.Y. Luo, T.X. Liang, and W.L. Guo, The Effects of Grain Refinement and Deformation on Corrosion Resistance of Passive Film Formed on the Surface of 304 Stainless Steels, *Mater. Res. Bull.*, 2015, **70**, p 896–907
  57. A.A. Aghuy, M. Zakeri, and M.H. Moayed, Effect of Grain Size on Pitting Corrosion of 304L Austenitic Stainless Steel, *Corros. Sci.*, 2015, **94**, p 368–376
  58. F.J. Humphreys, Review Grain and Subgrain Characterisation by Electron Backscatter Diffraction, *J. Mater. Sci.*, 2001, **36**, p 3833–3854
  59. E.A. Holm, G.S. Rohrer, S.M. Foiles, A.D. Rollett, H.M. Miller, and D.L. Olmsted, Validating Computed Grain Boundary Energies in FCC

- Metals Using the Grain Boundary Character Distribution, *Acta Mater.*, 2011, **59**, p 5250–5256
60. M.P. Phaniraj, D.I. Kim, and Y.W. Cho, Effect of Grain Boundary Characteristics on the Oxidation Behavior of Ferritic Stainless Steel, *Corros. Sci.*, 2011, **53**, p 4124–4130
  61. V. Randle, Twinning-related Grain Boundary Engineering, *Acta Mater.*, 2004, **52**, p 4067–4081
  62. W.T. Read and W. Shockley, Dislocation Models of Crystal Grain Boundaries, *Phys. Rev.*, 1950, **78**, p 275
  63. N. An and R. Herrmann, Distribution of the Atoms on Grain Boundaries and in the Bravais Cell of the Coincidence Site Lattice, *Phys. Status Solidi B*, 2010, **118**, p 691–702
  64. N. Sakaguchi, Y. Ohguchi, T. Shibayama, S. Watanabe, and H. Kinoshita, Surface Cracking on  $\Sigma 3$ ,  $\Sigma 9$  CSL and Random Grain Boundaries in Helium Implanted 316L Austenitic Stainless Steel, *J. Nucl. Mater.*, 2013, **432**, p 23–27
  65. M. Shimada, H. Kokawa, Z.J. Wang, Y.S. Sato, and I. Karibe, Optimization of Grain Boundary Character Distribution for Intergranular Corrosion Resistant 304 Stainless Steel by Twin-Induced Grain Boundary Engineering, *Acta Mater.*, 2002, **50**, p 2331–2341
  66. C. Hu, S. Xia, H. Li, T. Liu, B. Zhou, W.J. Chen, and N. Wang, Improving the Intergranular Corrosion Resistance of 304 Stainless Steel by Grain Boundary Network Control, *Corros. Sci.*, 2011, **53**, p 1880–1886
  67. L. Peguet, B. Malki, and B. Baroux, Effect of Austenite Stability on the Pitting Corrosion Resistance of Cold Worked Stainless Steels, *Corros. Sci.*, 2009, **51**, p 493–498
  68. S.K. Pradhan, P. Bhuyan, and S. Mandal, Influence of the Individual Microstructural Features on Pitting Corrosion in Type 304 Austenitic Stainless Steel, *Corros. Sci.*, 2019, **158**, p 108091
  69. H. Gao, Mechanism-Based Strain Gradient Plasticity I: Theory, *J. Mech. Phys. Solids*, 1999, **47**, p 1239–1263
  70. L.P. Kubin and A. Mortensen, Geometrically Necessary Dislocations and Strain-Gradient Plasticity: A Few Critical Issues, *Scr. Mater.*, 2003, **48**, p 119–125
  71. R.E. Schramm and R.P. Reed, Stacking Fault Energies of Seven Commercial Austenitic Stainless Steels, *Metall. Trans. A*, 1975, **6**, p 1345
  72. M.S. Pham, B. Dovgvy, and P.A. Hooper, Twinning Induced Plasticity in Austenitic Stainless Steel 316L Made by Additive Manufacturing, *Mater. Sci. Eng., A*, 2017, **704**, p 102–111
  73. M.S. Pham and S.R. Holdsworth, Dynamic Strain Ageing of AISI, 316L During Cyclic Loading at 300 °C: Mechanism, Evolution, and Its Effects, *Mater. Sci. Eng., A*, 2012, **556**, p 122–133

**Publisher's Note** Springer Nature remains neutral with regard to jurisdictional claims in published maps and institutional affiliations.